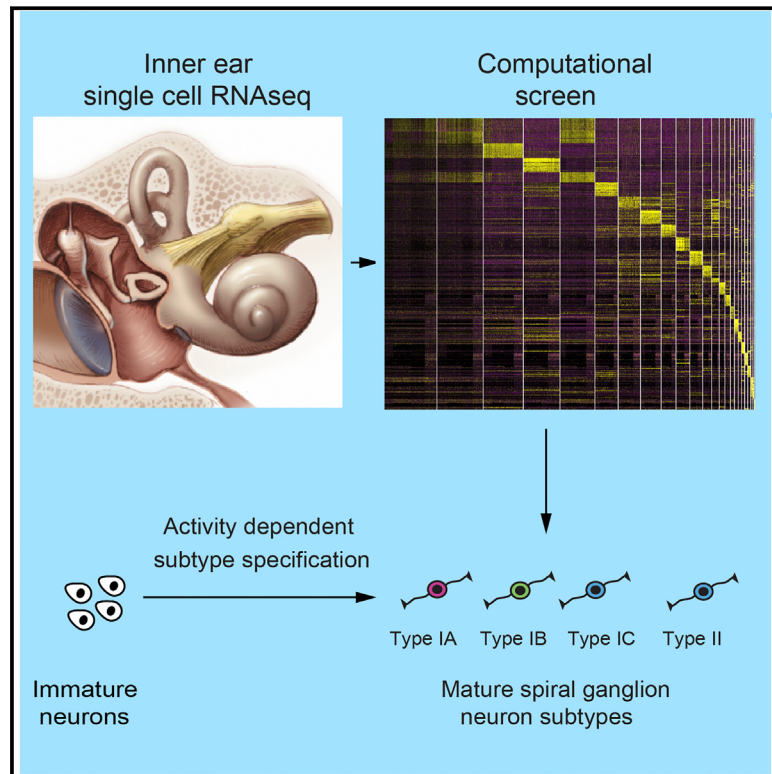


Hair Cell Mechanotransduction Regulates Spontaneous Activity and Spiral Ganglion Subtype Specification in the Auditory System

Graphical Abstract



Authors

Shuhao Sun, Travis Babola,
Gabriela Pregernig, ..., Dwight E. Bergles,
Joseph C. Burns, Ulrich Müller

Correspondence

jburns@decibeltx.com (J.C.B.),
umuelle3@jhmi.edu (U.M.)

In Brief

Single-cell analyses of mouse type I spiral ganglion neurons characterize three functionally distinct subtypes, revealing insights into auditory processing with implications for treating congenital deafness.

Highlights

- Single-cell RNA sequencing identifies subtypes of auditory sensory neurons
- Neuronal subtype specification is initiated in the pre-hearing period
- Activity-dependent processes regulate subtype specification
- Mechanotransduction channels regulate spontaneous activity pre-hearing

Hair Cell Mechanotransduction Regulates Spontaneous Activity and Spiral Ganglion Subtype Specification in the Auditory System

Shuhao Sun,^{1,3} Travis Babola,^{1,3} Gabriela Pregermig,^{2,3} Kathy S. So,² Matthew Nguyen,² Shin-San M. Su,² Adam T. Palermo,² Dwight E. Bergles,¹ Joseph C. Burns,^{2,*} and Ulrich Müller^{1,4,*}

¹The Solomon Snyder Department of Neuroscience and Department of Otolaryngology, Head and Neck Surgery, Johns Hopkins University School of Medicine, 725 N. Wolfe Street, Baltimore, MD 21205, USA

²Decibel Therapeutics, 1325 Boylston Street, Suite 500, Boston, MA 02215, USA

³These authors contributed equally

⁴Lead Contact

*Correspondence: jburns@decibeltx.com (J.C.B.), umuelle3@jhmi.edu (U.M.)

<https://doi.org/10.1016/j.cell.2018.07.008>

SUMMARY

Type I spiral ganglion neurons (SGNs) transmit sound information from cochlear hair cells to the CNS. Using transcriptome analysis of thousands of single neurons, we demonstrate that murine type I SGNs consist of subclasses that are defined by the expression of subsets of transcription factors, cell adhesion molecules, ion channels, and neurotransmitter receptors. Subtype specification is initiated prior to the onset of hearing during the time period when auditory circuits mature. Gene mutations linked to deafness that disrupt hair cell mechanotransduction or glutamatergic signaling perturb the firing behavior of SGNs prior to hearing onset and disrupt SGN subtype specification. We thus conclude that an intact hair cell mechanotransduction machinery is critical during the pre-hearing period to regulate the firing behavior of SGNs and their segregation into subtypes. Because deafness is frequently caused by defects in hair cells, our findings have significant ramifications for the etiology of hearing loss and its treatment.

INTRODUCTION

Hearing depends on the conversion of mechanical stimuli into electrical signals within the cochlea. The signaling capability of this sensory system is extraordinary, responding to sound-induced vibrations of atomic dimension, amplifying signals >100-fold, and having a large dynamic range that enables us to perceive sound over a broad intensity and frequency range. The mechano-electrical conversion critical for hearing is carried out by hair cells (Figure 1A). Three rows of outer hair cells (OHCs) amplify sound-induced vibrations that reach the cochlea. These vibrations induce deflection of stereocilia at the apical surface of inner hair cells (IHCs) (Figure 1A), open transduction channels in stereocilia, and lead to excitation of spiral ganglion

neurons (SGNs). Sound frequencies are relayed to the nervous system as a tonotopic map, with IHCs at the base of the cochlea responding to the highest frequencies and those at the apex to the lowest frequencies (Gillespie and Müller, 2009; Meyer and Moser, 2010).

IHCs and OHCs are innervated by SGNs, but with distinct synaptic organization. Type I SGNs exhibit input from only one IHC, whereas type II SGNs extend long projections and receive input from dozens of OHCs. Although IHCs exhibit one-to-one coupling with SGNs, each IHC is innervated mono-synaptically by 5–30 type I SGNs that transmit sound information to the CNS. Type I SGNs constitute 95% of all SGNs while the remaining 5% are the type II SGNs (Figure 1A) (Perkins and Morest, 1975; Ryugo, 1992; Spoendlin, 1973). Type II SGNs are not essential for transmission of sound information to the CNS and instead appear to have a role in damage perception and pain signaling (Flores et al., 2015; Liu et al., 2015). Like hair cells, type I SGNs are organized tonotopically and each SGN is most sensitive to one particular frequency, coinciding with its relative position along the cochlear partition (Davis and Crozier, 2015; Meyer and Moser, 2010). However, not all properties of SGNs vary tonotopically. The most sensitive region for hearing is in the middle part of the cochlea, while neurons in the apical and basal region are less sensitive (Heffner et al., 1994; Koay et al., 2002; Ruggero and Temchin, 2002).

In addition to this regional specificity, type I SGNs that innervate single IHCs also exhibit diverse characteristics (Heil and Peterson, 2015). Type I SGNs have variable spontaneous rates (SRs) that are inversely correlated with their threshold to sound and dynamic range (Liberman, 1978; Sachs and Abbas, 1974). Discharge rates from near 0 to 120 spikes per second have been observed. The distribution of SGNs with different SRs is largely bimodal with a peak at low rates (≤ 1 spike/s) and higher rates (60–70 spikes/s) in some species such as cats but not in rodents where nerve fibers show a gradual increase from low to high SRs (Heil and Peterson, 2015). Based on studies in cats, a classification of SGNs into three classes has been proposed: high-SR (>18 spikes/s), medium-SR (0.5–18 spikes/s), and low-SR (<0.5 spikes/s) fibers. This classification takes into account SRs and relative thresholds for activation by sensory input

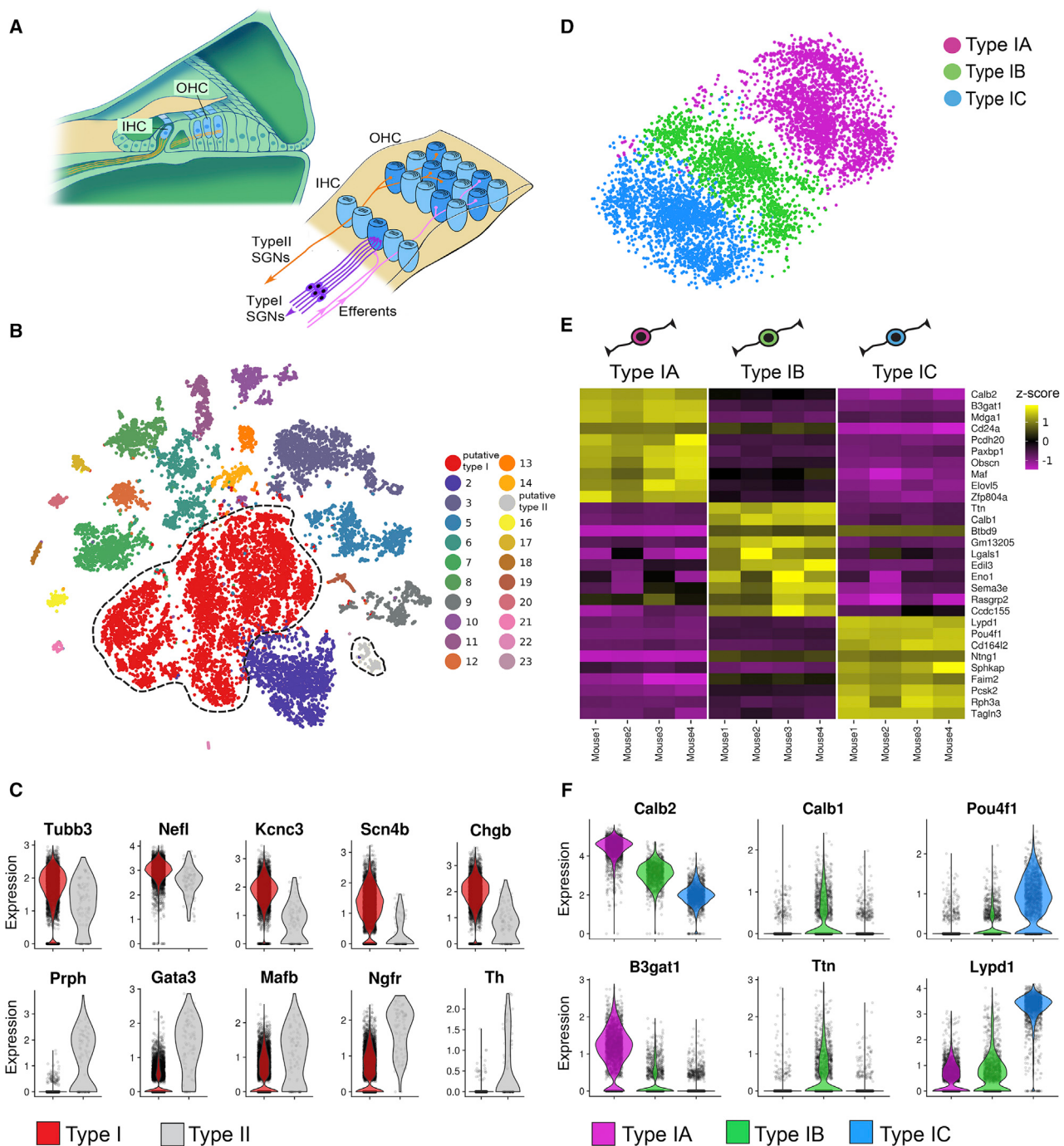


Figure 1. Identification of Subtype of Type I SGNs by scRNA-Seq

(A) Diagram on the left: cochlear cross-section; inner hair cells, IHCs; outer hair cells, OHCs. Right: top view onto the sensory epithelium showing IHCs, OHCs, and SGNs. Efferent neurons are shown in pink but are not studied here.

(B) tSNE plot from the sensory compartment of the mouse inner ear at 9 weeks of age. Putative type I SGNs (*Tubb3*⁺) in red; putative type II SGNs (*Prph*⁺) in gray.

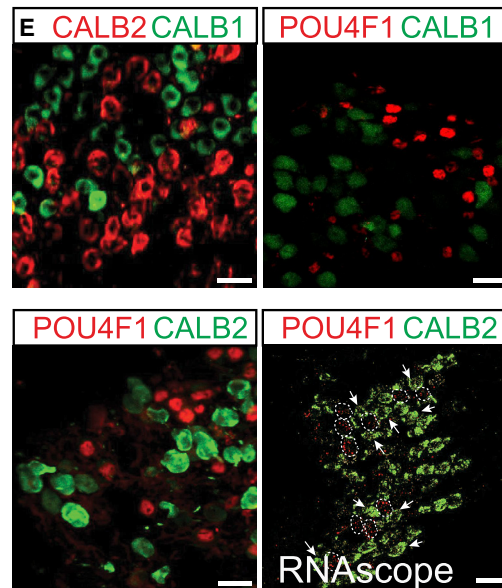
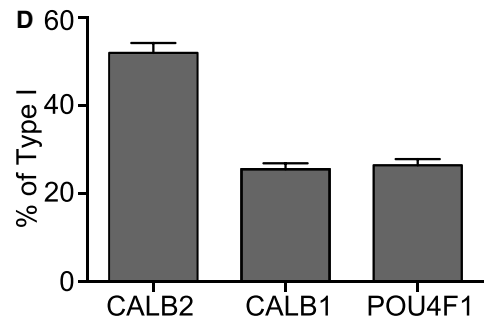
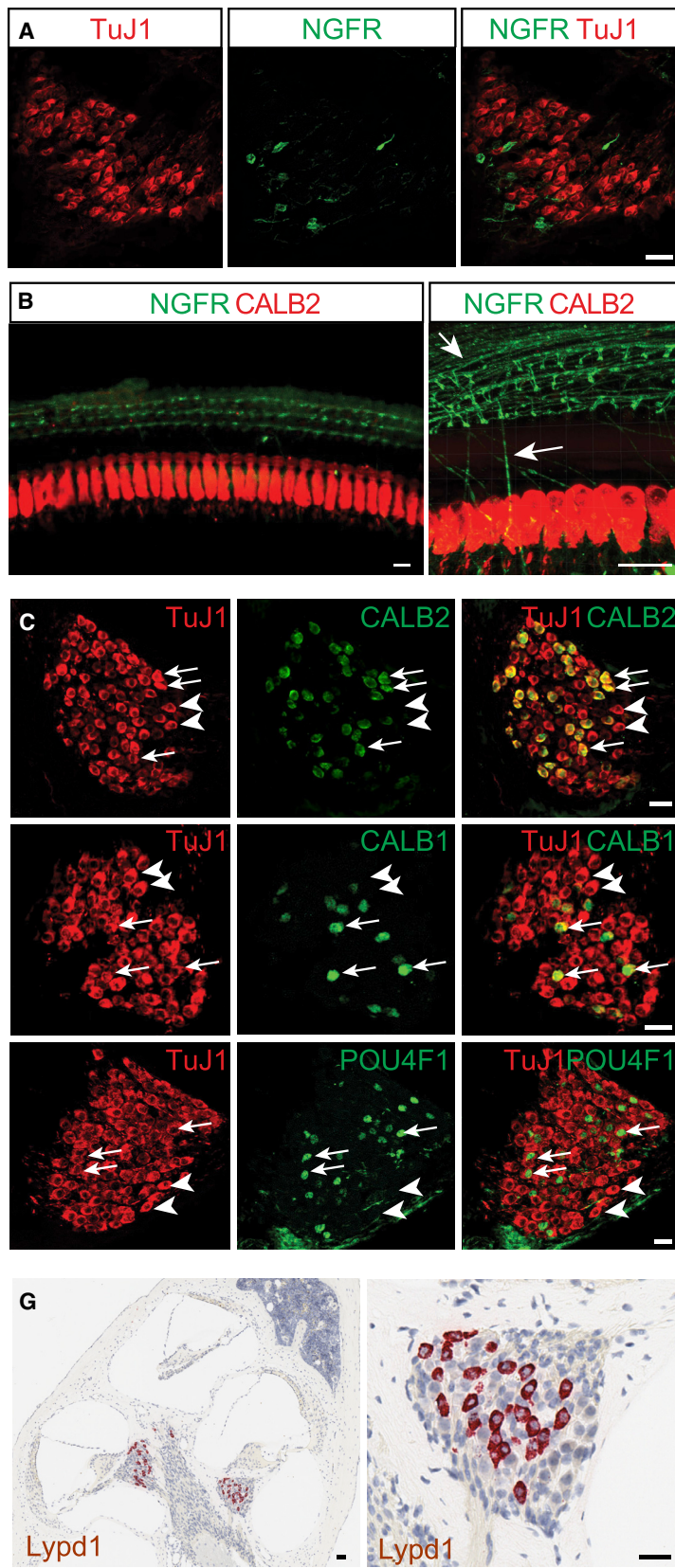
(C) Violin plots showing select genes that are differentially expressed between final sets of type I and type II SGNs (see Figures S5A and S5B and STAR Methods for SGNs refinement); y axis is a log scale.

(D) tSNE plot of type I SGNs showing three subtypes (IA, IB, IC).

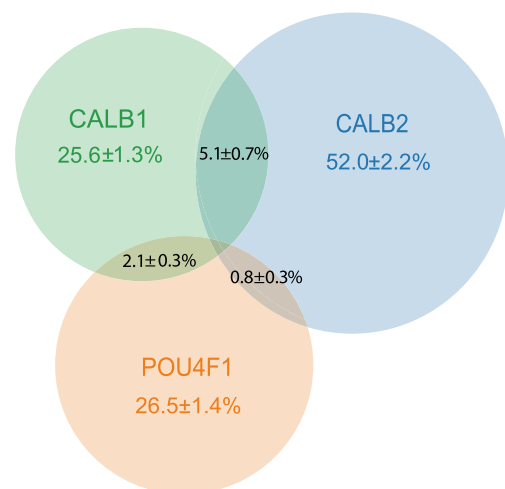
(E) Heatmaps showing standardized expression of the top 10 differentially expressed genes ($p < 0.01$ from pairwise comparisons, highest average log-fold change). Expression is averaged across all cells from an individual mouse for each cluster. Rows are genes, columns are averages for each mouse, grouped by cluster.

(F) Violin plots of select genes from (E) within subtypes. y axis in (C) and (F), log-normalized transcript counts.

See also Figures S1, S2, S3, S4, S5, S6, and S7, Tables S1, S2, S3, S4, S5, and S6, and the STAR Methods.



F



(legend on next page)

(Liberman, 1978). In cats, low- and high-SR fibers preferentially contact the modiolar and pillar sides of IHCs, respectively (Liberman, 1982). In rodents, single IHCs also appear to be innervated by fibers with different SRs (Liberman et al., 2011; Wu et al., 2016). This is compelling because it could allow for parallel information processing by functionally distinct neurons that receive input from a single hair cell.

Here, we analyzed molecular diversity within murine SGNs. Using massive parallel single-cell RNA sequencing (scRNA-seq), we demonstrate that type I SGNs are molecularly diverse and are comprised of three main subtypes, which can be subdivided into six classes. These molecularly distinct subtypes reach maturity postnatally when auditory circuits mature. Disruption of mechanotransduction channels in hair cells or glutamate release from hair cells affect spontaneous activity and subtype specification of SGNs prior to hearing onset, suggesting that activity patterns experienced by SGNs during this critical period influence their developmental trajectories. Our analysis of the molecular diversity of SGNs leads to the surprising conclusion that an intact mechanotransduction machinery is critical even in the pre-hearing period to promote spontaneous activity and molecular diversification of type I SGNs.

RESULTS

Identification of SGN Subtypes by Single-Cell RNA Sequencing

To molecularly profile SGNs, we carried out massively parallel scRNA-seq experiments with cells obtained from the inner ears of 9-week-old, male CBA/CaJ mice. We optimized the micro-dissection procedure to enrich for sensory neurons (see STAR Methods) and independently dissociated cells from four mice for use in droplet microfluidics (10X Genomics Chromium) to obtain cell-barcoded cDNAs that were sequenced. After filtering out low complexity droplets, the dataset consisted of 17,556 high quality cells (Figure S1; Table S1) (Macosko et al., 2015; Zheng et al., 2017).

Mature type I SGNs can be distinguished from type II SGNs by high levels of *Tubb3* expression while mature type II SGNs strongly express *Prph* (Barclay et al., 2011; Hafidi, 1998; Lallemand et al., 2007; Mou et al., 1998; Nishimura et al., 2017; Vyas et al., 2017). Unbiased clustering revealed groups of neurons that were separable on a t-distributed stochastic neighbor embedding (t-SNE) plot of all cells (Figure 1B). Based on expression of *Tubb3* and *Prph*, three of the clusters represented putative type I SGNs (red cells) and one cluster putative type II SGNs (gray cells) (Figures 1B, S2A, and S2C). SGNs comprised 40% (6,713) of the total cell number, confirming

that our micro-dissection enriched these neurons. The remaining cells consisted of at least 20 additional clusters (Figures 1B, S2A, S2B, and S3).

While the identity calling of putative SGNs was robust to a number of clustering parameter variations (Figure S4), non-neuronal cell types in the dataset could introduce biases into neuronal sub-clusters. Therefore, we selected the four putative groups of neurons and re-clustered the data in the absence of other cell types. After filtering out cells with undetermined identity (8%, Figure S5), 6,113 SGNs remained (see STAR Methods). In agreement with the expected relative contribution of the two types of neurons to the SGN pool (Perkins and Morest, 1975; Ryugo, 1992; Spoendlin, 1973), 98% and 2% of SGNs were assigned to the type I and type II identity, respectively.

1,616 genes were differentially expressed between type I and type II SGNs (absolute log fold-change > 0.1; adjusted p value < 0.01; Table S2). Top hits that were elevated in type II SGNs included known markers such as *Prph*, *Gata3*, *Mafb*, and *Th* (Barclay et al., 2011; Hafidi, 1998; Lallemand et al., 2007; Mou et al., 1998; Nishimura et al., 2017; Vyas et al., 2017). Genes that were significantly increased in type I SGNs included structural proteins (*Tubb3*, *Nefl*) and ion channels (*Kcnc3* and *Scn4b*) (Figure 1C).

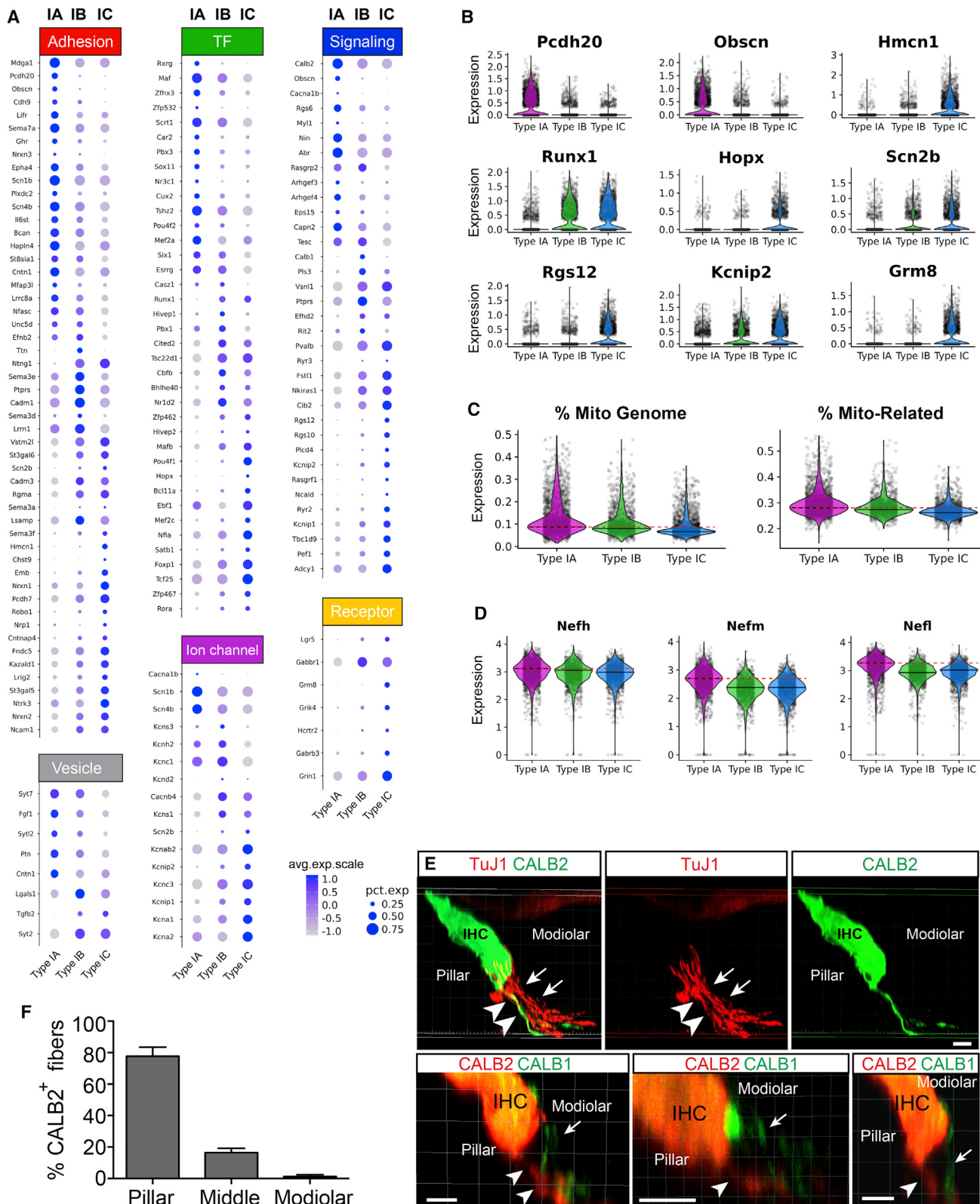
Three subtypes of type I SGNs can be distinguished in cats based on spontaneous rates of firing and sound detection thresholds (Liberman, 1978). We re-analyzed the putative type I SGNs, varying parameters to extract three clusters from the dataset that we named IA, IB, and IC (Figures 1D, S5, S6, and S7). Cluster IA contained 39% of the cells, cluster IB 27%, and cluster IC 34%. Cluster separation was driven by a host of genes and was reproducible across all four mice from which cells were obtained (Figures 1E, 1F, S7A, S7B, and S7F; Table S3). Most of the identified genes have not been shown to be expressed in subsets of SGNs. An exception is *Pou4f1*, which is confined to a subset of SGNs (Xiang et al., 1997).

A subset of the sequenced type I SGNs expressed significant levels of glial genes (Figure S6B). This was unsurprising, given that type I SGNs are myelinated. Glial fragments likely remained attached to the SGNs after dissociation. When we restricted our analysis to pure type I SGNs with very low expression levels of glial genes (clusters 4 and 5; Figures S6C and S6D), we recapitulated all of our main findings (Figures S6E–S6G; Tables S4 and S5). We also carried out differential expression analysis between purer SGNs and contaminated SGNs. Only a small percentage of genes differentially expressed between the subtypes corresponded to “contaminating genes” (Figure S6H).

While our data analysis was guided by reported electrophysiology findings, we explored whether there was additional

Figure 2. Validation of Molecular Subtypes of SGNs

- (A) P28 sections stained with antibodies to TuJ1 (red) and NGFR (green) to identify type I and type II SGNs.
(B) P28 cochlear whole mounts stained for CALB2 to label IHCs and for NGFR (green). Note labeling of type II nerve fibers (arrows) within the OHC region.
(C) P28 sections stained with the indicated antibodies to distinguish types IA, IB, and IC SGNs (arrowheads, cells only expressing TuJ1; arrows cells co-expressing TuJ1 with CALB2, CALB1, or POU4F1).
(D) Percentage of type I SGNs expressing CALB2, CALB1, and POU4F1 at P28 (serial sections from three mice; values are mean ± SEM).
(E) P28 sections stained for CALB2, CALB1, and POU4F1. In bottom right panel, segregation of markers as determined by RNAscope (arrows: Calb2⁺ cells).
(F) Quantification of the percentage of type I SGNs co-expressing markers (serial sections from three mice; values are mean ± SEM).
(G) RNAscope analysis of Lypd1 expression. Left: overview of the cochlea. Right: spiral ganglion. Scale bars, 20 μm.



(legend on next page)

SGN diversity. An alternative clustering procedure based on independent component analysis (ICA) and different parameters (see STAR Methods) split the cells into six clusters. This analysis revealed a set of genes that was expressed in a subset of cells from each of the previously identified groups (Figure S7).

Verification of SGN Subtypes

To verify the RNA profiling data, we analyzed the expression of putative markers for the type I SGNs subtypes defined by transcriptome analysis (Figures 1D–1F) by immunohistochemistry. TuJ1 distinguishes type I SGNs from type II SGNs (Barclay et al., 2011; Lallemend et al., 2007), and we identified NGFR as a type II SGN marker (Figure 1C). Immunostaining of histological sections at P28 revealed expression of TuJ1 in the majority of SGNs, with the exception of a smaller neuronal population at the periphery of the ganglion where type II SGNs tend to be localized (Figure 2A). These neurons at the periphery expressed high levels of NGFR (Figure 2A). Staining of whole mounts demonstrated that NGFR⁺ cells extended projections to OHCs, as predicted for type II SGNs (Figure 2B).

Next, sections were co-stained with antibodies to TuJ1 to identify type I SGNs and with antibodies to CALB2 (type IA), CALB1 (type IB), and POU4F1 (type IC). As predicted, high levels of CALB2, CALB1, and POU4F1 were expressed in subsets of SGNs (Figure 1C; 52% ± 2% CALB2⁺; 26% ± 1% CALB1⁺; 27% ± 1% POU4F1⁺) (Figure 2D). Double-immunofluorescence experiments confirmed that CALB2, CALB1, and POU4F1 (Figure 2E) labeled distinct SGN populations, with a small overlap between populations (Figures 2E and 2F).

We confirmed by RNAscope that *Lypd1* (type IC marker) was present in a subset of SGNs (Figure 2G), and that *Calb2* and *Pou4f1* were expressed in different SGN subpopulations (Figure 2E; 50% ± 3% *Pou4f1*⁺, 32% ± 2% *Calb2*⁺; overlap 4% ± 1%) in good agreement with the values obtained by immunohistochemistry (Figure 2F).

Contrasting Expression Patterns of Gene Families in SGN Subtypes

Neuronal subtypes in the cortex can be distinguished by the differential expression of members of gene families belonging to six categories (Table S6): (1) transcription factors (TFs); (2) cell-adhesion molecules (CAMs); (3) receptors for neurotransmitters and modulators; (4) voltage-gated ion channels; (5) regulatory signaling proteins; and (6) neuropeptides and vesicle release

machinery (Paul et al., 2017). We identified genes that were differentially expressed between subtypes for each class (Figures 3A and S7B; Table S3). Figure 3B shows violin plots for some of the genes, highlighting that while differences in gene expression were prominent between type IA, IB, and IC SGNs, they were not all-or-none. Differences in the expression of CAMs, cell signaling molecules, ion channels, and neurotransmitter receptors (Figure 3A), may reflect differences in the innervation pattern of IHCs by subtypes of SGNs and differences in synaptic connectivity and signaling mechanisms within the auditory nucleus. For example, *Grm8*, which encodes a metabotropic glutamate receptor, was highly expressed in type IC SGNs, but not in type IA and IB SGNs.

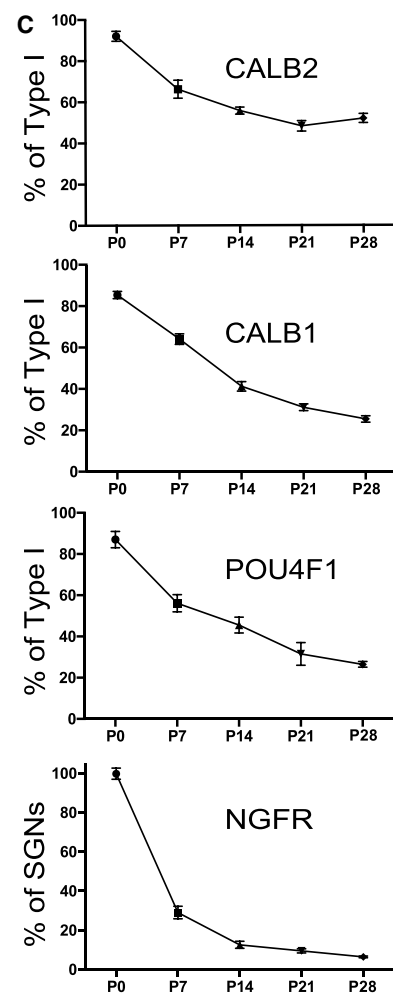
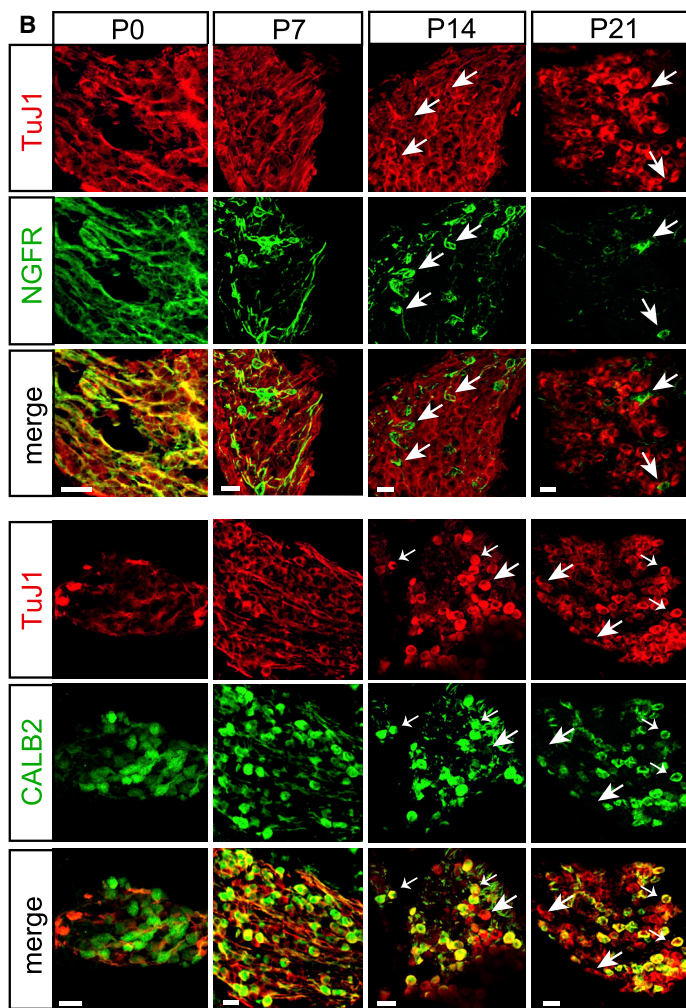
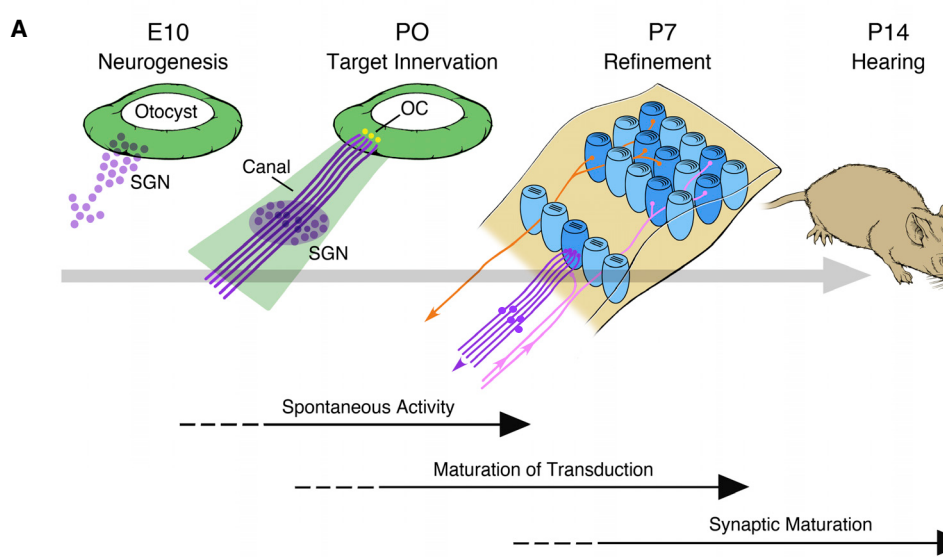
Innervation of Inner Hair Cells by Type I SGNs

In cats, high-SR neurons have an increased mitochondrial content and increased fiber thickness compared to low-SR and medium-SR fibers (Liberman, 1980; Merchan-Perez and Liberman, 1996). Low- and high-SR fibers in cats also preferentially contact the modiolar and pillar sides of IHCs, respectively (Liberman, 1982). In mice, SRs of type I SGNs also vary (Taberner and Liberman, 2005; Wu et al., 2016) and synaptic contacts at the modiolar and pillar side of IHCs show structural differences (Liberman et al., 2011). Intriguingly, type IA SGNs had elevated expression levels of genes associated with mitochondrial function compared to type IB and IC SGNs (Figure 3C) indicative of increased mitochondrial content. Type IA SGNs also expressed higher levels of neurofilament transcripts (Figure 3D), which correlates with an increased axonal diameter (Elder et al., 1998; Hoffman et al., 1987; Marszalek et al., 1996; Xu et al., 1996). Thus, type IA SGNs most closely correspond to high-SR fibers.

We also traced projections to IHCs. Cochlear whole mounts were immunostained for CALB2 and TuJ1, which are detectable in projections of type I SGNs (Figure 3E). CALB2 also labels IHCs (Figure 2B), thus allowing us to identify targets of type I SGNs. We collected serial optical sections through the sensory epithelium and generated 3D projections of 65 hair cells. The type I SGN marker TuJ1⁺ labeled all nerve fibers contacting the basal part of IHCs at the modiolar, middle, and pillar sides (Figures 3E and 3F). CALB2⁺ type IA SGN projections were prominent on the pillar side of IHCs, with some projections innervating the middle side (Figures 3E and 3F). Our CALB1 antibody occasionally revealed CALB1 expression in nerve fibers innervating IHCs.

Figure 3. Molecular Characterization of Type I SGN Subtypes and Innervation Patterns

- (A) Dot plots showing differentially expressed genes (\log_{10} fold-change > 0.1 and $p < 0.01$ from pairwise comparisons) in type I SGN subtypes grouped by functional category; color scale: average expression of all single cells in each cluster; dot size: percentage of single cells with detectable expression (> 1 transcript).
- (B) Violin plots of select genes.
- (C) Violin plots of fraction of total transcripts in single cells from the 13 protein-coding genes in the mitochondrial genome and 1,092 cellular genes associated with mitochondrial function (Calvo et al., 2016). All pairwise comparisons are statistically significant ($p < 0.0001$, nested model ANOVA).
- (D) Violin plots of neurofilament gene expression. Lines in (C) and (D) indicate the peak density of cells in the violin plots. The dotted line is an extension of the line from type IA neurons to facilitate comparison. y axis in (B) and (D), log-normalized transcript counts. y axis in (C), fraction of total transcripts in each single cell. The genes shown are differentially expressed between subtypes (\log_{10} fold-change > 0.1 ; $p < 0.01$ from pairwise comparisons).
- (E) 3D reconstructions of an IHC and innervating nerve endings at P28. Top: cochlear whole mounts stained for TuJ1 (red) to identify type I SGNs projections (arrows) and for CALB2 (green) to identify IHCs and type IA SGN projections (arrowheads). Bottom: whole mounts co-stained for CALB1 (green; arrows) and CALB2 (red; arrowheads).
- (F) 3D renderings (10 mice; 5–15 hair cells per sample) to quantify innervation patterns. We divided the base of IHCs into modiolar, middle, and pillar side according to the TuJ1 innervation area and quantified the number of cells where CALB2⁺ nerve fibers contacted IHCs. Values are mean \pm SEM. Scale bar, 8 μm .



(legend on next page)

CALB1⁺ fibers segregated from CALB2⁺ fibers and projected to the modiolar side of IHCs (Figure 3F). These findings indicate that type I SGN subtypes converge on single IHCs with distinct innervation patterns.

Subclasses of SGNs Are Specified Postnatally

We next asked whether molecular differences in type I SGNs were observed at the progenitor level or were detectable only subsequently within the maturing ganglion. SGNs in mice are born from progenitors in the otic vesicle and delaminate around embryonic day (E) 10 to form the spiral ganglion (Figure 4A). Postmitotic SGNs elaborate projections to hair cells by P0 and refine them during the first few postnatal weeks (Echteler, 1992; Huang et al., 2007, 2012; Koundakjian et al., 2007; Perkins and Morest, 1975; Simmons, 1994; Sobkowicz et al., 1986). Mechanotransduction currents in mouse hair cells are detected at birth and reach mature levels in 5–10 days (Kim and Fettiplace, 2013; Lelli et al., 2009; Pan et al., 2013). The onset of hearing in mice does not occur until P12–P14 (Ehret, 1983; Mikaelian and Ruben, 1965) and synapse formation between SGNs and hair cells progresses up to P28 (Figure 4A) (Huang et al., 2012; Liberman and Liberman, 2016; Sobkowicz et al., 1986). We therefore immunostained sections of the inner ear between P0 and P28 with markers for SGN subtypes.

NGFR, CALB2, CALB1, and POU4F1 were expressed at similar levels in essentially all SGNs at P0 (Figures 4B and 4C) but their expression was gradually refined at subsequent ages (Figure 4C). Type I SGNs could be distinguished from type II SGNs between P0–P7 (Figures 4B and 4C), but segregation of type I SGN markers continued up to P28 (Figures 4B and 4C). While we cannot exclude molecular differences between SGNs in prenatal animals, postmitotic SGNs undergo a major refinement in molecular phenotype in the first few postnatal weeks.

Specification of SGNs Is Affected by Mutations that Block Mechanotransduction Channels

Spontaneous and sensory input driven activity promotes the maturation and connectivity of neuronal circuits. To test whether activity-dependent mechanisms influence the specification of subtypes of SGNs, we analyzed mice with mutations in genes encoding components of the mechanotransduction machinery of hair cells. Mechanotransduction in hair cells depends on tip links and an associated ion channel complex containing LHPL5, TMIE, and TMC1/2 (Figure 5A) (Zhao and Müller, 2015). Mutations in *Tmie* and the tip-link component *Pcdh15* abolish transduction (Alagramam et al., 2011; Zhao et al., 2014), while *Lhfp5* mutations reduce transduction by ~90% (Xiong et al., 2012). Histological sections were prepared from mice carrying mutations in *Pcdh15*, *Lhfp5*, and *Tmie* between P0–P28 and analyzed for the expression of SGN subtype markers. Quantification of total SGN numbers at P28 revealed no

difference between wild-type and mutants, suggesting that SGN survival was not affected by the mutations under study up to P28 (Figure 5D). In mice deficient in *Pcdh15* and *Tmie*, adding the percentage of TuJ1⁺ neurons expressing CALB2, CALB1, or POU4F1 gave values well over 100% (Figures 5B and 5C), suggesting that specification of type IA, IB, and IC SGN subtypes was affected, resulting in co-expression of markers that typically define type I SGN subtypes. Expression of subtype markers was affected less severely in *Lhfp5* mutants (Figures 5C and 5D), consistent with the reduction, but not elimination, of mechanotransduction currents in *Lhfp5* mutants (Xiong et al., 2012). Co-immunolocalization studies with antibodies that mark type IA, IB, and IC SGNs in mice with mutations in *Pcdh15* and *Tmie* confirmed a large increase in the number of neurons co-expressing markers for type IA, IB, and IC SGNs (Figure 5E).

Analysis of the expression of TuJ1 (type I SGNs) and NGFR (type II SGNs) revealed a 2- to 4-fold increase in the percentage of NGFR⁺ SGNs in *Pcdh15*, *Tmie*, and *Lhfp5* mutants (Figures 5F and 5G). Less than 5% of NGFR expressing SGNs co-express TuJ1 in wild-type mice, while in *Pcdh15*, *Tmie* and *Lhfp5* mutant mice the number was increased by 4- to 10-fold (Figures 5F and 5G).

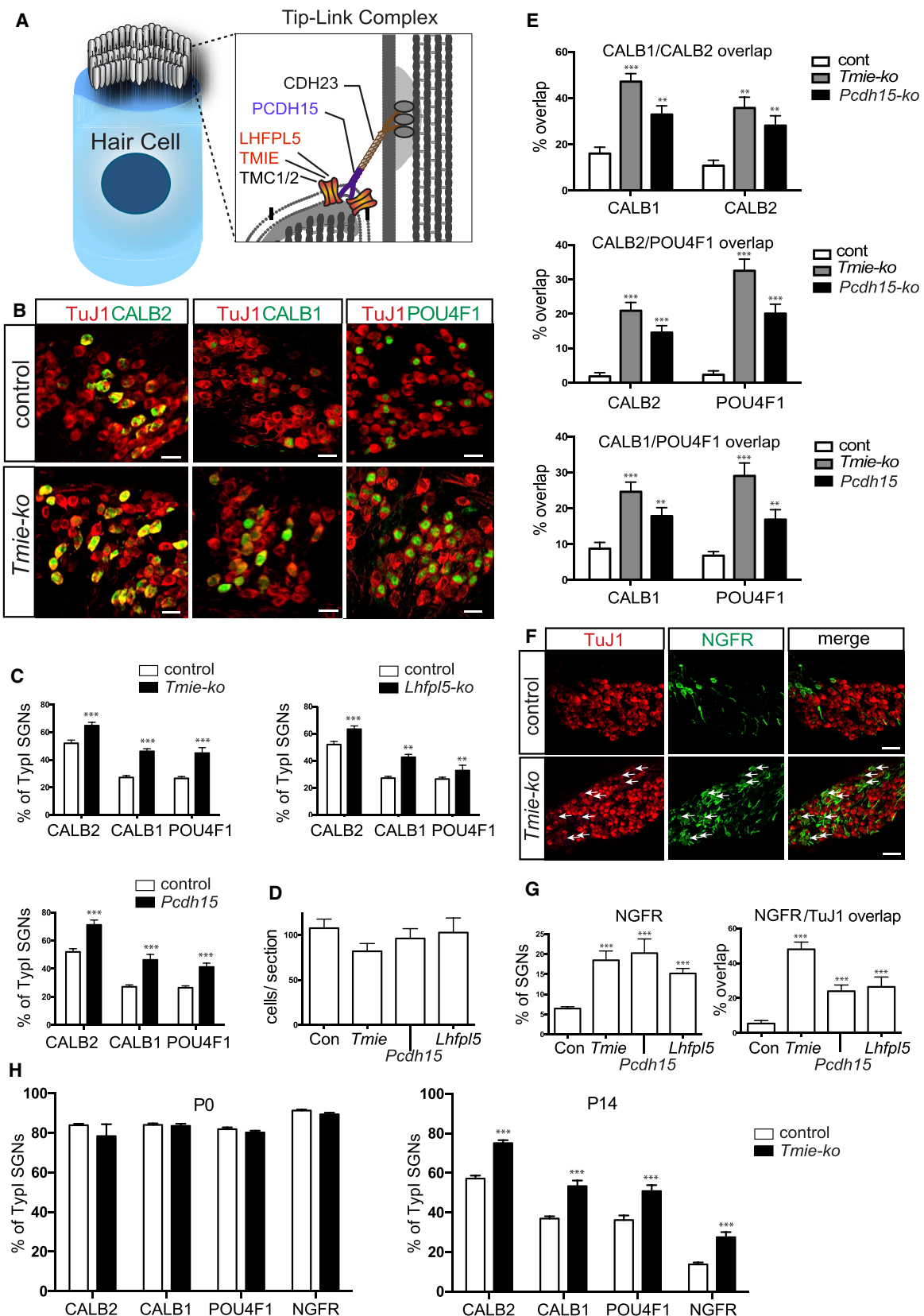
These findings suggest that disruption of mechanotransduction in IHCs and OHCs impairs proper segregation of type I and type II SGNs, as well as specification of type I SGNs into subclasses. Analysis of the developmental time course in *Tmie*-ko mice confirmed that defects in the segregation of molecular markers that identify SGN subtypes were apparent at hearing onset (P14; Figure 5H). We conclude that functional mechanotransduction is important for SGN specification at stages prior to hearing onset.

Specification of SGNs Is Disrupted by Mutations that Block Glutamatergic Signaling

Glutamatergic synaptic communication between IHCs and type I SGNs depends on the glutamate transporter VGLUT3 (Figure 6A) (Ruel et al., 2008; Seal et al., 2008). Glutamate release from hair cells prior to hearing onset is also involved in generating spontaneous activity in the developing auditory system (Tritsch et al., 2007; Wang et al., 2015). If activity-dependent processes participate in SGN specification, then disruption of this transporter should affect SGN development. Analysis of sections from *Vglut3* knockout (*Vglut3*-ko) mice (Seal et al., 2008) demonstrated that the expression pattern of SGN subtype markers was strikingly altered in the mutants, but in patterns that differed from mice with defects in mechanotransduction. The percentage of CALB1⁺ and CALB2⁺ neurons was increased in *Vglut3*-ko mice, and the percentage of POU4F1⁺ neurons was reduced (Figures 6A–6C). Total numbers of SGNs were also decreased at P28 in *Vglut3*-ko mice, although they were not different between wild-type and mutants at birth (Figure 6D). Because

Figure 4. Temporal Specification of SGN Subtypes

- (A) Diagram showing sequential steps during the maturation of the peripheral auditory sense organ.
(B) Histological section through the spiral ganglion were stained with the indicated antibodies (large arrows, single-positive cells; small arrows, double-positive cells).
(C) Quantification of the % of cells expressing different molecular markers at the indicated time points (serial sections from three mice at each time point; values are mean ± SEM). Scale bars, 20 μm.



(legend on next page)

SGNs are postmitotic at birth, these findings suggest that some neurons in *Vglut3*-ko mice had died postnatally.

We also observed in *Vglut3*-ko mice a large increase in the number of neurons co-expressing markers for type IA, IB, and IC SGNs (Figure 6E), as well as markers for type I and type II SGNs. The defects in subtype specification were detectable in *Vglut3*-ko mice at P14 (Figure 6H), providing evidence that they were established in the pre-hearing period. These data suggest that in the absence of glutamatergic signaling, molecular, and functional diversification between subtypes of type I SGNs and between type I and type II SGNs was affected.

SGNs Exhibit Altered Patterns of Activity in *Tmie*-ko and *Vglut3*-ko Mice

SGNs fire discrete bursts of action potentials prior to hearing onset, due to periodic depolarization of IHCs by K⁺ released from inner supporting cells (ISCs) (Figures 7A and 7B) (Tritsch et al., 2007; Wang et al., 2015). To determine if loss of *Tmie* or *Vglut3* alters SGN activity during this period, we examined the firing behavior of SGNs in cochlear whole-mounts at P5–P7. Juxtacellular recordings (Figure 7A) revealed that SGNs in *Tmie*-ko mice continued to exhibit spontaneous activity, with action potentials grouped into bursts (Figures 7B and 7C), but had lower activity rates than controls (Figures 7D and 7E), with lower average frequencies of individual action potentials and bursts (Figure 7F). Burst duration and number of action potentials per burst also trended lower in *Tmie*-ko mice but did not reach significance (Figure 7F), while the timing of action potentials within bursts was similar between *Tmie*-ko and controls (Figure 7G) (Sonntag et al., 2009; Tritsch et al., 2010). However, there were fewer short interspike intervals (5–10 ms) in SGNs from *Tmie*-ko mice. These short intervals occur because each IHC Ca²⁺ spike typically triggers multiple action potentials with short intervals (i.e., a mini-burst) (Tritsch et al., 2010). This reduction in action potentials per mini-burst suggests that SGNs in *Tmie*-ko mice are less excitable than controls or that IHCs release less glutamate in response to each Ca²⁺ spike, thus leading to changes in the pattern of spontaneous activity. Application of the mechanotransduction channel inhibitor d-tubocurarine (d-TC, 50 μM) reduced the frequency and duration of bursts, as well as the average spike frequency (Figure 7F), mimicking patterns of activity observed in *Tmie*-ko mice, indicating that these changes in activity primarily reflect the contribution of mechanotransduction channels.

Postsynaptic AMPA receptor-mediated currents are absent in *Vglut3*-ko mice (Seal et al., 2008). As glutamatergic transmission is required for the excitation of SGNs prior to hearing onset (Tritsch et al., 2007; Zhang-Hooks et al., 2016), we predicted that SGNs

should not exhibit periodic bursts of action potentials in *Vglut3*-ko mice. Unexpectedly, juxtacellular recordings revealed that SGNs continued to exhibit spontaneous firing in *Vglut3*-ko mice (Figure 7I). SGN bursts were less distinct in *Vglut3*-ko mice than in controls (Figures 7H–7K), and although bursts were longer they contained fewer spikes (Figure 7J). Mini-bursts were also absent in *Vglut3*-ko mice (Figure 7K), as expected if IHC Ca²⁺ spikes are no longer responsible for inducing SGN firing (Tritsch et al., 2010). Thus, loss of IHC-SGN synaptic communication does not abolish periodic burst firing of SGNs prior to hearing onset but induces distinct activity patterns. In vivo imaging studies show that these changes in activity patterns in *Vglut3*-ko mice are propagated throughout the auditory system (Babola et al., 2018).

We conclude that genetic disruption of two IHC genes involved in sensory transduction, *Tmie* and *Vglut3*, lead to distinct changes in the activity and molecular specification of SGNs prior to hearing onset, suggesting that the firing pattern exhibited by SGNs during this period plays a crucial role in guiding the molecular and functional maturation of the auditory system.

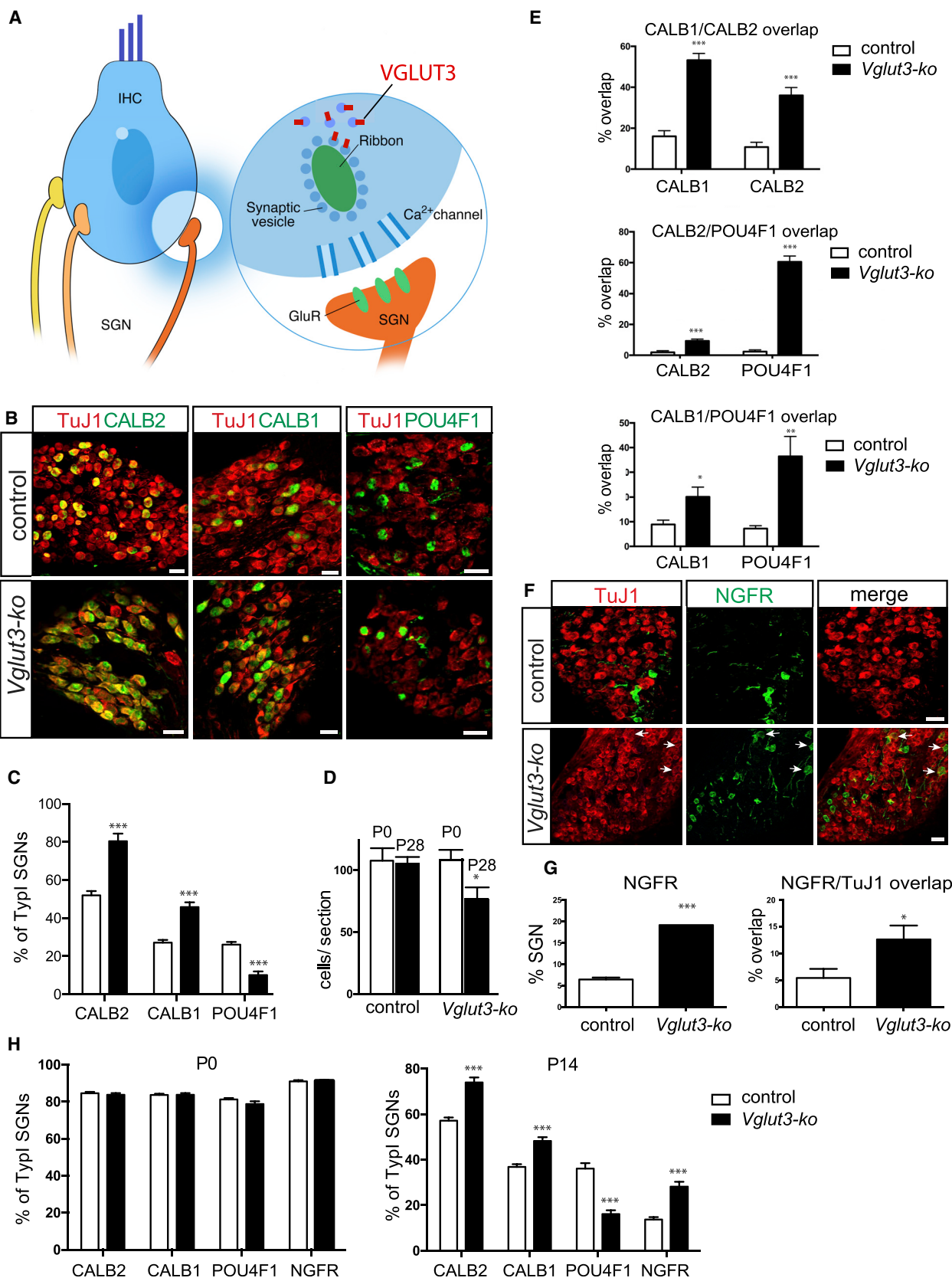
DISCUSSION

Here, we provide a comprehensive characterization of the gene expression program of SGNs, identify molecularly distinct SGN subtypes, and demonstrate that activity-dependent mechanisms are critical for SGN subtype specification. Previous studies had identified several genes that are expressed at different levels in mature type I and type II SGNs (Barclay et al., 2011; Hafidi, 1998; Lallemand et al., 2007; Mou et al., 1998; Nishimura et al., 2017; Vyas et al., 2017), and we have identified many more. The functional consequences of these differences need to be explored, but one gene, *Ngfr*, provides an interesting example. *Ngfr* is highly expressed in type II SGNs. *Ngfr* encodes the low-affinity p75 neurotrophin receptor, which also interacts with tropomyosin kinase (Trk) receptors to modulate ligand binding to these high-affinity neurotrophin receptors (Huang and Reichardt, 2003). Neurotrophins regulate cochlear innervation by type I SGNs via Trks (Fritzsch et al., 1997), but the role of p75 in the inner ear is less clear. p75 when expressed in the absence of Trks can activate cell death pathways (Lu et al., 2005) and p75 is upregulated in the inner ear in response to injury (Tan and Shepherd, 2006). The difference in p75 expression might indicate differences in the response of type I and type II SGNs to neurotrophins.

Our findings reveal differences in the expression of a wide range of genes in type I SGNs suggesting that these neurons are functionally diverse and consisting of three major subtypes.

Figure 5. Defects in Hair Cell Mechanotransduction Affects SGN Subtype Specification

- (A) Hair cell diagram. Inset: enlargement of the tip-link region indicating molecules of the mechanotransduction complex.
- (B) Sections through the spiral ganglion of control wild-type mice and *Tmie*-ko mice at P28 stained with the indicated antibodies.
- (C) Numbers of CALB2⁺, CALB1⁺, and POU4F1⁺ SGNs in wild-type, *Tmie*-ko, *Lhfp15*-ko, and *Pcdh15*-av3j mice at P28.
- (D) Quantification of SGN numbers at P28.
- (E) Numbers of CALB2⁺, CALB1⁺, and POU4F1⁺ SGNs at P28. Total numbers of double-positive cells were divided by numbers of cell expressing a single marker.
- (F) Histological sections of wild-type and *Tmie*-ko mice at P28 stained with the indicated antibodies (arrows, cells co-expressing TuJ1 and NGFR).
- (G) Numbers of NGFR⁺ and NGFR⁺/TuJ1⁺ SGNs at P28.
- (H) Numbers of CALB2⁺, CALB1⁺, POU4F1⁺, and NGFR⁺ SGNs in mice of the indicated genotype at P0 and P14. For all experiments, serial sections from three animals of each genotype were analyzed. Values are mean ± SEM; two-tailed unpaired t test; ***p < 0.001; **p < 0.01; *p < 0.05. Scale bars, 20 μm.



(legend on next page)

These subtypes were also identified in a parallel study (Shrestha et al., 2018; this issue of *Cell*) and might correspond to the three functional subtypes of type I SGNs proposed by Liberman (1978) based on electrophysiological criteria and threshold of activation to sound. Type IA neurons most closely resemble high-SR fibers in cats, a conclusion that was also reached by the Goodrich laboratory (Shrestha et al., 2018). Like high-SR fibers, type IA neurons innervate IHCs on the pillar side and express elevated levels of mitochondrial genes and neurofilament genes indicative of increased mitochondrial content and axonal diameter.

When we applied alternative clustering methods to our data, we identified six subtypes of type I SGNs, suggesting greater diversity in this neuronal population than previously anticipated. Even in species where neurons have been grouped according to SR rates, SR rates vary even within groups (Heil and Peterson, 2015). Furthermore, type I SGNs are organized tonotopically and neurons innervating the middle part of the murine cochlea show the lowest thresholds of activation by sound and highest resting membrane potentials (Liu and Davis, 2007; Liu et al., 2014). Thus, some of the observed molecular differences might reflect additional differences in the physiological properties of SGNs.

Our findings suggest that activity-dependent mechanisms are critical for the diversification of SGNs. Action potentials that occur independent of external input have been observed in the nervous system and they affect both cell proliferation and differentiation (Arroyo and Feller, 2016; Cohen-Cory, 2002; Huberman et al., 2008; Kandler, 2004; Wang and Bergles, 2015). In the auditory system, brain stem circuitry shows sensory-input independent activity coincident with structural and functional maturation (Kandler et al., 2009; Kandler and Gillespie, 2005; Tritsch and Bergles, 2010; Tritsch et al., 2007; Wang et al., 2015). Despite the immaturity of ribbon synapses at early postnatal stages, IHCs excite SGNs through activation of their glutamate receptors (Beutner and Moser, 2001; Glowatzki and Fuchs, 2002; Johnson et al., 2005; Robertson and Paki, 2002; Tritsch and Bergles, 2010; Wang and Bergles, 2015). Inner supporting cells are implicated in the generation of spontaneous activity in the cochlea (Tritsch et al., 2007; Wang et al., 2015), but the involvement of IHC in this process are less well understood.

Our findings show that active mechanotransduction channels in hair cells are critical for shaping spontaneous firing patterns in SGNs before hearing onset. Previous studies have shown that spontaneous release of ATP initiates IHC excitation at early postnatal ages to induce glutamate release from IHCs. ATP release induces crenations in supporting cells surrounding hair cells (Tritsch et al., 2007). These crenations could provide a mechanical stimulus to hair cells leading to the activation of mechanotransduction

channels in the prehearing period, amplifying the direct depolarization of SGNs produced by K^+ release from inner supporting cells.

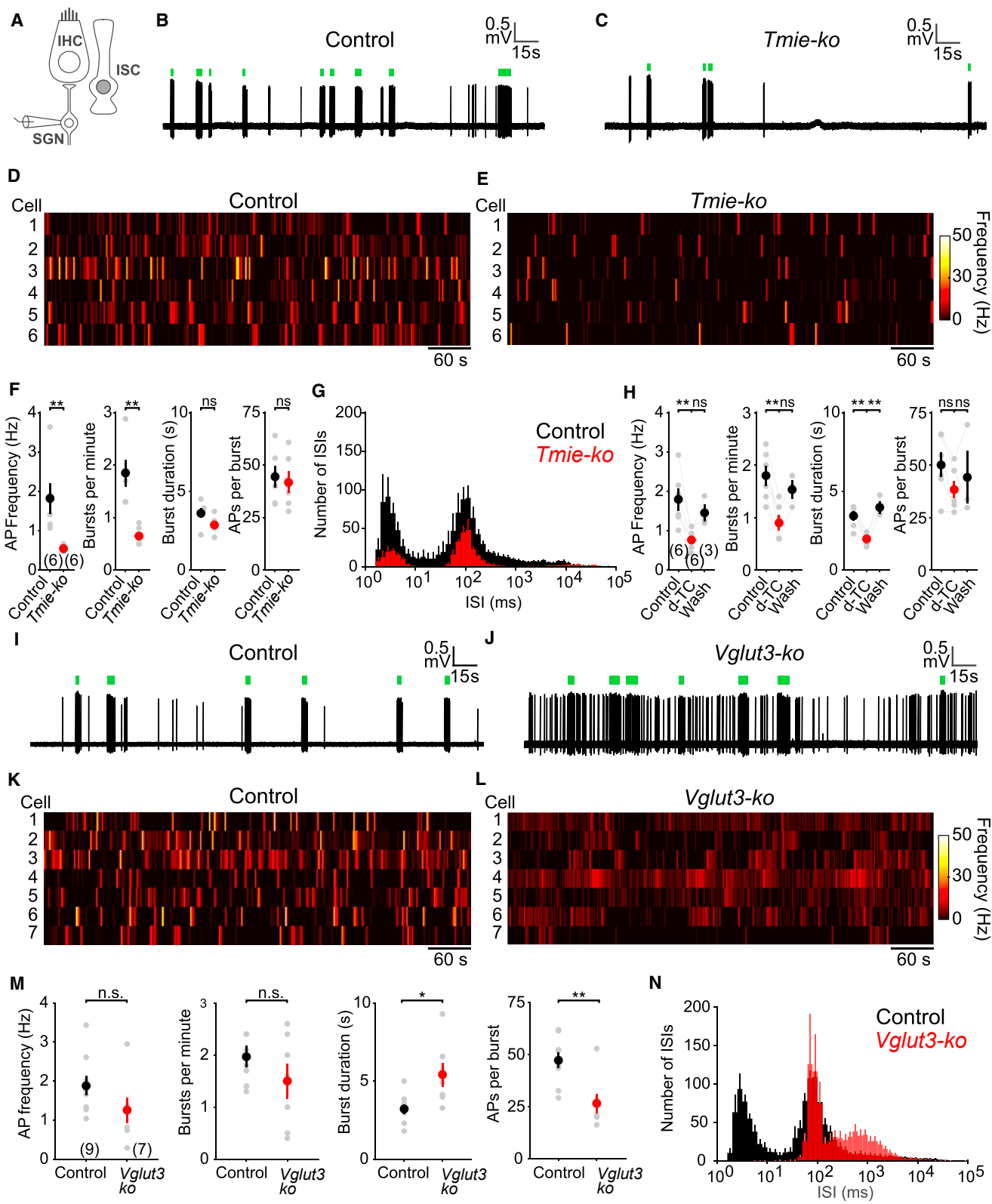
Perturbations of mechanotransduction channels and glutamate release affected the spontaneous activity of SGNs and their subtype specification, suggesting that the two events are linked. Consistent with this model, subtype specification of SGNs was initiated in the pre-hearing period coincident with the time-frame when spontaneous activity in SGNs is observed. Refinement of SGN subtypes continues into the fourth week after birth, thus extending into the time of active hearing, suggesting that sensory input driven events also participate in SGN specification. Maturation of ribbon synapses continues until the fourth postnatal week (Huang et al., 2012; Liberman and Liberman, 2016; Sobkowicz et al., 1986). This time-frame also overlaps with the period when murine SGNs refine their firing properties from an immature state to a range of fibers differing in their SRs (Wu et al., 2016), indicating an intricate interplay between molecular and functional diversification.

Disruption of mechanotransduction in IHCs and OHCs and glutamate release from IHCs affected spontaneous activity patterns and SGN subtype specification in distinct ways. In the absence of mechanotransduction, bursts of action potentials are reduced. Neurons do not die (at least up to P28), but increased numbers of SGNs continue to co-express markers for subtypes of type I SGNs suggesting that they remain immature. In contrast, inactivation of *Vglut3* changed the pattern of spontaneous activity to longer bursts with fewer spikes, altered SGN subtype specification and caused loss predominantly of one type I SGN subtype. How can the differences be explained? Glutamate release may regulate SGN survival and glutamate may still be released from hair cells even in the absence of mechanotransduction channels, but not when VGLUT3 is absent. Other mechanisms might also be at play. Notably, inactivation of *Vglut3* is thought to only affects IHCs, while mutations in *Pcdh15*, *Tmie*, and *Lhfp15* affect both IHCs and OHCs. In each instance, increased numbers of neurons co-express type I and type II markers suggesting that the maturation of both principal SGN subtypes is affected. During development, nerve fibers of type II SGNs bypass IHCs while type I SGNs innervate IHCs. SGNs elaborate excessive branches that are subsequently refined (Echteler, 1992; Huang et al., 2007, 2012; Koundakjian et al., 2007; Perkins and Morest, 1975; Simmons, 1994; Sobkowicz et al., 1986). This refinement process is perhaps dependent on activity-dependent mechanisms.

Hearing loss is the most common form of sensory impairment in humans. More than 70 genes have been linked to the disease and mutations in many genes disrupt hair cell function (Dror and Avraham, 2010; Richardson et al., 2011). Our findings predict

Figure 6. Defects in Glutamatergic Signaling by IHCs Affects SGN Subtype Specification

- (A) Diagram of an IHC with innervating type I SGNs. Inset: enlargement of a ribbon synapse between IHCs and SGNs. Glutamate receptors (GluR) localizes to nerve terminals and VGLUT3 to vesicles.
- (B) Section through the spiral ganglion of control wild-type mice and *Vglut3-ko* mice at P28 stained with the indicated antibodies.
- (C) Numbers of CALB2⁺, CALB1⁺, and POU4F1⁺ SGNs in wild-type and mutants at P28.
- (D) Quantification of SGN numbers at P28.
- (E) Numbers of CALB2⁺, CALB1⁺, and POU4F1⁺ SGNs at P28. Total numbers of double-positive cells were divided by numbers of cell expressing a single marker.
- (F) Histological sections of wild-type and *Vglut3-ko* mice at P28 stained with the indicated antibodies.
- (G) Numbers of Ngfr⁺ and Ngfr⁺/Tuj1⁺ SGNs at P28.
- (H) Numbers of CALB2⁺, CALB1⁺, POU4F1⁺, and Ngfr⁺ SGNs in mice of the indicated genotype at P0 and P14. For all experiments, serial sections from three animals of each genotype were analyzed. Values are mean \pm SEM; two tailed unpaired t test; ***p < 0.001; **p < 0.01; *p < 0.05. Scale bars, 20 μ m.



(legend on next page)

that hair cell defects will secondarily affect the development of auditory circuitry. Significantly, hearing loss has also been proposed to be caused by loss of synaptic innervation of IHCs by SGNs (Liberman, 2017). Low-SR synapses seem to be particularly vulnerable to noise or aging (Furman et al., 2013; Schmiedt et al., 1996). Recent findings suggest that the type IC neurons are lost in aging mice (Shrestha et al., 2018), lending further support to the notion that they might correspond to low-SR fibers. It will be important to determine in more detail the extent to which the specific SGN subtypes are affected by noise and aging, and whether IHC activity at adult ages is required to maintain the proper distribution of type I SGN subtypes.

STAR★METHODS

Detailed methods are provided in the online version of this paper and include the following:

- KEY RESOURCES TABLE
- CONTACT FOR REAGENT AND RESOURCE SHARING
- EXPERIMENTAL MODEL AND SUBJECT DETAILS
 - Ethic statement
 - Mouse strains
- METHOD DETAILS
 - Cell dissociation of SGNs for single-cell RNA-Seq
 - Single-cell capture, library preparation, and RNA-Seq
 - Processing and QC of single-cell RNA-Seq data
 - Dimensionality reduction and clustering
 - Classification of type I and type II SGNs
 - Clustering robustness
 - Classification of type I SGN subtypes
 - Differential expression analysis
 - Effects of glial contamination
 - Immunofluorescence
 - RNAscope *in situ* hybridization
 - Electrophysiology
- DATA AND SOFTWARE AVAILABILITY

SUPPLEMENTAL INFORMATION

Supplemental Information includes seven figures and six tables and can be found with this article online at <https://doi.org/10.1016/j.cell.2018.07.008>.

Figure 7. SGNs in *Tmie-ko* and *Vglut3-ko* Mice Exhibit Altered Burst Firing before Hearing Onset

- (A) Diagram showing the juxtacellular recording configuration used to assess SGNs. ISC, inner supporting cell.
- (B and C) Spontaneous action potentials from SGNs in control mice (*Tmie*^{+/+} or *Tmie*^{+/-} littermates) (B) and *Tmie-ko* mice (C). Green bars indicate discrete action potential bursts.
- (D and E) Raster plots indicating the average firing rate of SGNs (bin: 1 s) in control mice (D) and *Tmie-ko* mice (E).
- (F) Quantification of average action potential (AP) frequency, frequency, and duration of spontaneous bursts, and number of action potentials per burst from control and *Tmie-ko* mice.
- (G) Average log-binned interspike interval (ISI) histograms from control and *Tmie-ko* mice.
- (H) Quantification of average action potential frequency, frequency and duration of spontaneous bursts, and number of action potentials per burst from cochleae treated with d-tubocurarine (d-TC; 50 µM).
- (I and J) Spontaneous action potentials recorded from SGNs of control mice (*Vglut3*^{+/+} or *Vglut3*^{+/-} littermates) (I) and *Vglut3-ko* mice (J). Green bars indicate discrete action potential bursts.
- (K and L) Raster plots indicating average SGN firing rates (bin: 1 s) in control mice (K) and *Vglut3-ko* mice (L).
- (M) Quantification of average action potential frequency, frequency and duration of spontaneous bursts, and number of action potentials per burst in cochleae from control and *Vglut3-ko* mice. All values are mean ± SEM. Statistical significance calculated with two-tailed paired t test, Bonferroni correction applied; **p < 0.01, *p < 0.05, ns, not significant.
- (N) Average log-binned interspike interval (ISI) histograms from control and *Vglut3-ko* mice.

ACKNOWLEDGMENTS

This research was funded by NIDCD (DC005965, DC007704, and DC014713 to U.M. and DC008060 to D.E.B.) and a grant from the Rubenstein Fund for Hearing Research (D.E.B. and U.M.).

AUTHOR CONTRIBUTIONS

All authors contributed to experimental design and data analysis. RNA-seq and data analysis were carried out by G.P., A.T.P., K.S.S., S.-S.M.S., and J.C.B. Analysis of mice by histology was carried out by S.S. M.N. contributed RNAscope data. Spontaneous activity was evaluated by T.B. and D.E.B. U.M., J.C.B., S.S., and G.P. wrote the manuscript with input from all authors.

DECLARATION OF INTERESTS

J.C.B., S.-S.M.S., A.T.P., G.P., M.N., and K.S.S. are employees of Decibel Therapeutics. U.M. is a co-founder of Decibel Therapeutics and a member of its scientific advisory board.

Received: February 22, 2018

Revised: April 23, 2018

Accepted: July 2, 2018

Published: August 2, 2018

REFERENCES

- Alagramam, K.N., Goodyear, R.J., Geng, R., Furness, D.N., van Aken, A.F., Marcotti, W., Kros, C.J., and Richardson, G.P. (2011). Mutations in protocadherin 15 and cadherin 23 affect tip links and mechanotransduction in mammalian sensory hair cells. *PLoS ONE* 6, e19183.
- Arroyo, D.A., and Feller, M.B. (2016). Spatiotemporal features of retinal waves instruct the wiring of the visual circuitry. *Front. Neural Circuits* 10, 54.
- Babola, T.A., Li, S., Gribizis, A., Lee, B.J., Issa, J.B., Wang, H.C., Crair, M.C., and Bergles, D.E. (2018). Homeostatic control of spontaneous activity in the developing auditory system. *Neuron* 99. Published online August 1, 2018. <https://doi.org/10.1016/j.neuron.2018.07.004>.
- Barclay, M., Ryan, A.F., and Housley, G.D. (2011). Type I vs type II spiral ganglion neurons exhibit differential survival and neuritogenesis during cochlear development. *Neural Dev.* 6, 33.
- Beutner, D., and Moser, T. (2001). The presynaptic function of mouse cochlear inner hair cells during development of hearing. *J. Neurosci.* 21, 4593–4599.
- Borgius, L., Restrepo, C.E., Leao, R.N., Saleh, N., and Kiehn, O. (2010). A transgenic mouse line for molecular genetic analysis of excitatory glutamatergic neurons. *Mol. Cell. Neurosci.* 45, 245–257.

- Butler, A., Hoffman, P., Smibert, P., Papalex, E., and Satija, R. (2018). Integrating single-cell transcriptomic data across different conditions, technologies, and species. *Nat. Biotechnol.* 36, 411–420.
- Calvo, S.E., Clouser, K.R., and Mootha, V.K. (2016). MitoCarta2.0: an updated inventory of mammalian mitochondrial proteins. *Nucleic Acids Res.* 44 (D1), D1251–D1257.
- Cohen-Cory, S. (2002). The developing synapse: construction and modulation of synaptic structures and circuits. *Science* 298, 770–776.
- D'Alessandro, A., Righetti, P.G., and Zolla, L. (2010). The red blood cell proteome and interactome: an update. *J. Proteome Res.* 9, 144–163.
- Davis, R.L., and Crozier, R.A. (2015). Dynamic firing properties of type I spiral ganglion neurons. *Cell Tissue Res.* 361, 115–127.
- Dobin, A., Davis, C.A., Schlesinger, F., Drenkow, J., Zaleski, C., Jha, S., Batut, P., Chaisson, M., and Gingeras, T.R. (2013). STAR: ultrafast universal RNA-seq aligner. *Bioinformatics* 29, 15–21.
- Dror, A.A., and Avraham, K.B. (2010). Hearing impairment: a panoply of genes and functions. *Neuron* 68, 293–308.
- Echteler, S.M. (1992). Developmental segregation in the afferent projections to mammalian auditory hair cells. *Proc. Natl. Acad. Sci. USA* 89, 6324–6327.
- Ehret, G. (1983). Development of hearing and response to behavior to sound stimuli: behavioral studies. In *Development of the auditory and vestibular systems* Academic, R. Romand, ed. (Academic Press, New York), pp. 211–237.
- Elder, G.A., Friedrich, V.L., Jr., Kang, C., Bosco, P., Gurov, A., Tu, P.H., Zhang, B., Lee, V.M., and Lazzarini, R.A. (1998). Requirement of heavy neurofilament subunit in the development of axons with large calibers. *J. Cell Biol.* 143, 195–205.
- Finak, G., McDavid, A., Yajima, M., Deng, J., Gersuk, V., Shalek, A.K., Slichter, C.K., Miller, H.W., McElrath, M.J., Prlic, M., et al. (2015). MAST: a flexible statistical framework for assessing transcriptional changes and characterizing heterogeneity in single-cell RNA sequencing data. *Genome Biol.* 16, 278.
- Flores, E.N., Duggan, A., Madathany, T., Hogan, A.K., Márquez, F.G., Kumar, G., Seal, R.P., Edwards, R.H., Liberman, M.C., and García-Añoveros, J. (2015). A non-canonical pathway from cochlea to brain signals tissue-damaging noise. *Curr. Biol.* 25, 606–612.
- Fritzsch, B., Silos-Santiago, I., Bianchi, L.M., and Fariñas, I. (1997). The role of neurotrophic factors in regulating the development of inner ear innervation. *Trends Neurosci.* 20, 159–164.
- Furman, A.C., Kujawa, S.G., and Liberman, M.C. (2013). Noise-induced cochlear neuropathy is selective for fibers with low spontaneous rates. *J. Neurophysiol.* 110, 577–586.
- Gillespie, P.G., and Müller, U. (2009). Mechanotransduction by hair cells: models, molecules, and mechanisms. *Cell* 139, 33–44.
- Glowatzki, E., and Fuchs, P.A. (2002). Transmitter release at the hair cell ribbon synapse. *Nat. Neurosci.* 5, 147–154.
- Hafidi, A. (1998). Peripherin-like immunoreactivity in type II spiral ganglion cell body and projections. *Brain Res.* 805, 181–190.
- Heffner, H.E., Heffner, R.S., Contos, C., and Ott, T. (1994). Audiogram of the hooded Norway rat. *Hear. Res.* 73, 244–247.
- Heil, P., and Peterson, A.J. (2015). Basic response properties of auditory nerve fibers: a review. *Cell Tissue Res.* 361, 129–158.
- Hoffman, P.N., Cleveland, D.W., Griffin, J.W., Landes, P.W., Cowan, N.J., and Price, D.L. (1987). Neurofilament gene expression: a major determinant of axonal caliber. *Proc. Natl. Acad. Sci. USA* 84, 3472–3476.
- Huang, E.J., and Reichardt, L.F. (2003). Trk receptors: roles in neuronal signal transduction. *Annu. Rev. Biochem.* 72, 609–642.
- Huang, L.C., Thorne, P.R., Housley, G.D., and Montgomery, J.M. (2007). Spatiotemporal definition of neurite outgrowth, refinement and retraction in the developing mouse cochlea. *Development* 134, 2925–2933.
- Huang, L.C., Barclay, M., Lee, K., Peter, S., Housley, G.D., Thorne, P.R., and Montgomery, J.M. (2012). Synaptic profiles during neurite extension, refinement and retraction in the developing cochlea. *Neural Dev.* 7, 38.
- Huberman, A.D., Feller, M.B., and Chapman, B. (2008). Mechanisms underlying development of visual maps and receptive fields. *Annu. Rev. Neurosci.* 39, 479–509.
- Johnson, S.L., Marcotti, W., and Kros, C.J. (2005). Increase in efficiency and reduction in Ca²⁺ dependence of exocytosis during development of mouse inner hair cells. *J. Physiol.* 563, 177–191.
- Kandler, K. (2004). Activity-dependent organization of inhibitory circuits: lessons from the auditory system. *Curr. Opin. Neurobiol.* 14, 96–104.
- Kandler, K., and Gillespie, D.C. (2005). Developmental refinement of inhibitory sound-localization circuits. *Trends Neurosci.* 28, 290–296.
- Kandler, K., Clause, A., and Noh, J. (2009). Tonotopic reorganization of developing auditory brainstem circuits. *Nat. Neurosci.* 12, 711–717.
- Kim, K.X., and Fettiplace, R. (2013). Developmental changes in the cochlear hair cell mechanotransducer channel and their regulation by transmembrane channel-like proteins. *J. Gen. Physiol.* 141, 141–148.
- Koay, G., Heffner, R., and Heffner, H. (2002). Behavioral audiograms of homozygous med(J) mutant mice with sodium channel deficiency and unaffected controls. *Hear. Res.* 171, 111–118.
- Koundakjian, E.J., Appler, J.L., and Goodrich, L.V. (2007). Auditory neurons make stereotyped wiring decisions before maturation of their targets. *J. Neurosci.* 27, 14078–14088.
- Lallemand, F., Vandenbosch, R., Hadjab, S., Bodson, M., Breuskin, I., Moonen, G., Lefebvre, P.P., and Malgrange, B. (2007). New insights into peripherin expression in cochlear neurons. *Neuroscience* 150, 212–222.
- Lelli, A., Asai, Y., Forge, A., Holt, J.R., and Gélécoc, G.S. (2009). Tonotopic gradient in the developmental acquisition of sensory transduction in outer hair cells of the mouse cochlea. *J. Neurophysiol.* 101, 2961–2973.
- Liberman, M.C. (1978). Auditory-nerve response from cats raised in a low-noise chamber. *J. Acoust. Soc. Am.* 63, 442–455.
- Liberman, M.C. (1980). Morphological differences among radial afferent fibers in the cat cochlea: an electron-microscopic study of serial sections. *Hear. Res.* 3, 45–63.
- Liberman, M.C. (1982). Single-neuron labeling in the cat auditory nerve. *Science* 216, 1239–1241.
- Liberman, M.C. (2017). Noise-induced and age-related hearing loss: new perspectives and potential therapies. *F1000Res.* 6, 927.
- Liberman, L.D., and Liberman, M.C. (2016). Postnatal maturation of auditory-nerve heterogeneity, as seen in spatial gradients of synapse morphology in the inner hair cell area. *Hear. Res.* 339, 12–22.
- Liberman, L.D., Wang, H., and Liberman, M.C. (2011). Opposing gradients of ribbon size and AMPA receptor expression underlie sensitivity differences among cochlear-nerve/hair-cell synapses. *J. Neurosci.* 31, 801–808.
- Liu, Q., and Davis, R.L. (2007). Regional specification of threshold sensitivity and response time in CBA/Caj mouse spiral ganglion neurons. *J. Neurophysiol.* 98, 2215–2222.
- Liu, Q., Lee, E., and Davis, R.L. (2014). Heterogeneous intrinsic excitability of murine spiral ganglion neurons is determined by Kv1 and HCN channels. *Neuroscience* 257, 96–110.
- Liu, C., Glowatzki, E., and Fuchs, P.A. (2015). Unmyelinated type II afferent neurons report cochlear damage. *Proc. Natl. Acad. Sci. USA* 112, 14723–14727.
- Lu, B., Pang, P.T., and Woo, N.H. (2005). The yin and yang of neurotrophin action. *Nat. Rev. Neurosci.* 6, 603–614.
- Macosko, E.Z., Basu, A., Satija, R., Nemesh, J., Shekhar, K., Goldman, M., Tirosh, I., Bialas, A.R., Kamitaki, N., Martersteck, E.M., et al. (2015). Highly parallel genome-wide expression profiling of individual cells using nanoliter droplets. *Cell* 161, 1202–1214.
- Madisen, L., Zwingman, T.A., Sunkin, S.M., Oh, S.W., Zariwala, H.A., Gu, H., Ng, L.L., Palmiter, R.D., Hawrylycz, M.J., Jones, A.R., et al. (2010). A robust

- and high-throughput Cre reporting and characterization system for the whole mouse brain. *Nat. Neurosci.* 13, 133–140.
- Marszalek, J.R., Williamson, T.L., Lee, M.K., Xu, Z., Hoffman, P.N., Becher, M.W., Crawford, T.O., and Cleveland, D.W. (1996). Neurofilament subunit NF-H modulates axonal diameter by selectively slowing neurofilament transport. *J. Cell Biol.* 135, 711–724.
- Merchan-Perez, A., and Liberman, M.C. (1996). Ultrastructural differences among afferent synapses on cochlear hair cells: correlations with spontaneous discharge rate. *J. Comp. Neurol.* 371, 208–221.
- Meyer, A.C., and Moser, T. (2010). Structure and function of cochlear afferent innervation. *Curr. Opin. Otolaryngol. Head Neck Surg.* 18, 441–446.
- Mikaelian, D., and Ruben, R.J. (1965). Development of hearing in the normal Cba-J mouse: correlation of physiological observations with behavioral responses and with cochlear anatomy. *Acta Otolaryngol.* 59, 451–461.
- Mou, K., Adamson, C.L., and Davis, R.L. (1998). Time-dependence and cell-type specificity of synergistic neurotrophin actions on spiral ganglion neurons. *J. Comp. Neurol.* 402, 129–139.
- Nishimura, K., Noda, T., and Dabdoub, A. (2017). Dynamic Expression of Sox2, Gata3, and Prox1 during primary auditory neuron development in the mammalian cochlea. *PLoS ONE* 12, e0170568.
- Pan, B., Gélécoc, G.S., Asai, Y., Horwitz, G.C., Kurima, K., Ishikawa, K., Kawashima, Y., Griffith, A.J., and Holt, J.R. (2013). TMC1 and TMC2 are components of the mechanotransduction channel in hair cells of the mammalian inner ear. *Neuron* 79, 504–515.
- Paul, A., Crow, M., Raudales, R., He, M., Gillis, J., and Huang, Z.J. (2017). Transcriptional architecture of synaptic communication delineates GABAergic neuron identity. *Cell* 171, 522–539.
- Perkins, R.E., and Morest, D.K. (1975). A study of cochlear innervation patterns in cats and rats with the Golgi method and Nomarkschi Optics. *J. Comp. Neurol.* 163, 129–158.
- Richardson, G.P., de Monvel, J.B., and Petit, C. (2011). How the genetics of deafness illuminates auditory physiology. *Annu. Rev. Physiol.* 73, 311–334.
- Robertson, D., and Paki, B. (2002). Role of L-type Ca²⁺ channels in transmitter release from mammalian inner hair cells. II. Single-neuron activity. *J. Neurophysiol.* 87, 2734–2740.
- Robertson, N.G., Resendes, B.L., Lin, J.S., Lee, C., Aster, J.C., Adams, J.C., and Morton, C.C. (2001). Inner ear localization of mRNA and protein products of COCH, mutated in the sensorineural deafness and vestibular disorder, DFNA9. *Hum. Mol. Genet.* 10, 2493–2500.
- Ruel, J., Emery, S., Nouvian, R., Bersot, T., Amilhon, B., Van Rybroek, J.M., Rebillard, G., Lenoir, M., Eybalin, M., Delprat, B., et al. (2008). Impairment of SLC17A8 encoding vesicular glutamate transporter-3, VGLUT3, underlies nonsyndromic deafness DFNA25 and inner hair cell dysfunction in null mice. *Am. J. Hum. Genet.* 83, 278–292.
- Ruggero, M.A., and Temchin, A.N. (2002). The roles of the external, middle, and inner ears in determining the bandwidth of hearing. *Proc. Natl. Acad. Sci. USA* 99, 13206–13210.
- Ryugo, D.K. (1992). The auditory nerve: peripheral innervation cell body morphology, and central projections. In *The Mammalian Auditory Pathway: Neuroanatomy*, A.N. Popper and R.R. Fay, eds. (New York: Springer), pp. 34–93.
- Sachs, M.B., and Abbas, P.J. (1974). Rate versus level functions for auditory-nerve fibers in cats: tone-burst stimuli. *J. Acoust. Soc. Am.* 56, 1835–1847.
- Satija, R., Farrell, J.A., Gennert, D., Schier, A.F., and Regev, A. (2015). Spatial reconstruction of single-cell gene expression data. *Nat. Biotechnol.* 33, 495–502.
- Schmiedt, R.A., Mills, J.H., and Boettcher, F.A. (1996). Age-related loss of activity of auditory-nerve fibers. *J. Neurophysiol.* 76, 2799–2803.
- Seal, R.P., Akil, O., Yi, E., Weber, C.M., Grant, L., Yoo, J., Clause, A., Kandler, K., Noebels, J.L., Glowatzki, E., et al. (2008). Sensorineural deafness and seizures in mice lacking vesicular glutamate transporter 3. *Neuron* 57, 263–275.
- Shrestha, B.R., Chia, C., Wu, L., Kujawa, S.G., Liberman, M.C., and Goodrich, L.V. (2018). Sensory neuron diversity in the inner ear is shaped by activity. *Cell* 174. Published online August 2, 2018. <https://doi.org/10.1016/j.cell.2018.07.007>.
- Simmons, D.D. (1994). A transient afferent innervation of outer hair cells in the postnatal cochlea. *Neuroreport* 5, 1309–1312.
- Sobkowicz, H.M., Rose, J.E., Scott, G.L., and Levenick, C.V. (1986). Distribution of synaptic ribbons in the developing organ of Corti. *J. Neurocytol.* 15, 693–714.
- Sonntag, M., Englitz, B., Kopp-Scheinplug, C., and Rübsamen, R. (2009). Early postnatal development of spontaneous and acoustically evoked discharge activity of principal cells of the medial nucleus of the trapezoid body: an in vivo study in mice. *J. Neurosci.* 29, 9510–9520.
- Spoedlin, H. (1973). The innervation of the cochlea receptor. In *Mechanisms in Hearing*, A.R. Moller, ed. (New York: Academic), pp. 185–229.
- Taberner, A.M., and Liberman, M.C. (2005). Response properties of single auditory nerve fibers in the mouse. *J. Neurophysiol.* 93, 557–569.
- Tan, J., and Shepherd, R.K. (2006). Aminoglycoside-induced degeneration of adult spiral ganglion neurons involves differential modulation of tyrosine kinase B and p75 neurotrophin receptor signaling. *Am. J. Pathol.* 169, 528–543.
- Trapnell, C., Cacchiarelli, D., Grimsby, J., Pokharel, P., Li, S., Morse, M., Lennon, N.J., Livak, K.J., Mikkelsen, T.S., and Rinn, J.L. (2014). The dynamics and regulators of cell fate decisions are revealed by pseudotemporal ordering of single cells. *Nat. Biotechnol.* 32, 381–386.
- Tritsch, N.X., and Bergles, D.E. (2010). Developmental regulation of spontaneous activity in the Mammalian cochlea. *J. Neurosci.* 30, 1539–1550.
- Tritsch, N.X., Yi, E., Gale, J.E., Glowatzki, E., and Bergles, D.E. (2007). The origin of spontaneous activity in the developing auditory system. *Nature* 450, 50–55.
- Tritsch, N.X., Rodríguez-Contreras, A., Crins, T.T., Wang, H.C., Borst, J.G., and Bergles, D.E. (2010). Calcium action potentials in hair cells pattern auditory neuron activity before hearing onset. *Nat. Neurosci.* 13, 1050–1052.
- Ubink, R., Calza, L., and Hökfelt, T. (2003). ‘Neuro’-peptides in glia: focus on NPY and galanin. *Trends Neurosci.* 26, 604–609.
- Vyas, P., Wu, J.S., Zimmerman, A., Fuchs, P., and Glowatzki, E. (2017). Tyrosine hydroxylase expression in type II cochlear afferents in mice. *J. Assoc. Res. Otolaryngol.* 18, 139–151.
- Wang, H.C., and Bergles, D.E. (2015). Spontaneous activity in the developing auditory system. *Cell Tissue Res.* 361, 65–75.
- Wang, H.C., Lin, C.C., Cheung, R., Zhang-Hooks, Y., Agarwal, A., Ellis-Davies, G., Rock, J., and Bergles, D.E. (2015). Spontaneous activity of cochlear hair cells triggered by fluid secretion mechanism in adjacent support cells. *Cell* 163, 1348–1359.
- Weskamp, G., and Reichardt, L.F. (1991). Evidence that biological activity of NGF is mediated through a novel subclass of high affinity receptors. *Neuron* 6, 649–663.
- Wu, J.S., Young, E.D., and Glowatzki, E. (2016). Maturation of spontaneous firing properties after hearing onset in rat auditory nerve fibers: spontaneous rates, refractoriness, and interfiber correlations. *J. Neurosci.* 36, 10584–10597.
- Xiang, M., Gan, L., Li, D., Chen, Z.Y., Zhou, L., O’Malley, B.W., Jr., Klein, W., and Nathans, J. (1997). Essential role of POU-domain factor Brn-3c in auditory and vestibular hair cell development. *Proc. Natl. Acad. Sci. USA* 94, 9445–9450.
- Xiong, W., Grillet, N., Elledge, H.M., Wagner, T.F., Zhao, B., Johnson, K.R., Kazmierczak, P., and Müller, U. (2012). TMHS is an integral component of the mechanotransduction machinery of cochlear hair cells. *Cell* 151, 1283–1295.
- Xu, Z., Marszalek, J.R., Lee, M.K., Wong, P.C., Folmer, J., Crawford, T.O., Hsieh, S.T., Griffin, J.W., and Cleveland, D.W. (1996). Subunit composition of neurofilaments specifies axonal diameter. *J. Cell Biol.* 133, 1061–1069.

- Zeisel, A., Muñoz-Manchado, A.B., Codeluppi, S., Lönnerberg, P., La Manno, G., Juréus, A., Marques, S., Munguba, H., He, L., Betsholtz, C., et al. (2015). Brain structure. Cell types in the mouse cortex and hippocampus revealed by single-cell RNA-seq. *Science* 347, 1138–1142.
- Zhang-Hooks, Y., Agarwal, A., Mishina, M., and Bergles, D.E. (2016). NMDA receptors enhance spontaneous activity and promote neuronal survival in the developing cochlea. *Neuron* 89, 337–350.
- Zhao, B., and Müller, U. (2015). The elusive mechanotransduction machinery of hair cells. *Curr. Opin. Neurobiol.* 34, 172–179.
- Zhao, B., Wu, Z., Grillet, N., Yan, L., Xiong, W., Harkins-Perry, S., and Müller, U. (2014). TMIE is an essential component of the mechanotransduction machinery of cochlear hair cells. *Neuron* 84, 954–967.
- Zheng, G.X., Terry, J.M., Belgrader, P., Ryvkin, P., Bent, Z.W., Wilson, R., Ziraldo, S.B., Wheeler, T.D., McDermott, G.P., Zhu, J., et al. (2017). Massively parallel digital transcriptional profiling of single cells. *Nat. Commun.* 8, 14049.
- Zheng, S., Papalex, E., Butler, A., Stephenson, W., and Satija, R. (2018). Molecular transitions in early progenitors during human cord blood hematopoiesis. *Mol. Syst. Biol.* 14, e8041.

STAR★METHODS

KEY RESOURCES TABLE

REAGENT or RESOURCE	SOURCE	IDENTIFIER
Antibodies		
goat anti-Calretinin (CALB2)	Swant	RRID: AB_10000342
mouse anti-Calretinin (CALB2)	Millipore	RRID: AB_94259
mouse anti-Tuj1	Biolegend	RRID: AB_2313773
rabbit anti-Tuj1	Sigma	RRID: AB_10743647
mouse anti-Neuronal nuclei	Chemicon	RRID: AB_2298772
mouse anti-Pou4f1	Millipore	RRID: AB_94166
rabbit anti-Calbindin (CALB1)	New England Biolabs	RRID: AB_2687400
rabbit anti-Tyrosine Hydroxylase	Millipore	RRID: AB_696697
rabbit anti-p75 NGFR	Weskamp and Reichardt, 1991	N/A
goat anti-rabbit Alexa 488 conjugated	Thermo Fisher	RRID: AB_143165
goat anti-rabbit Alexa 568 conjugated	Thermo Fisher	RRID: AB_143157
goat anti-mouse Alexa 488 conjugated	Thermo Fisher	RRID: AB_2534069
goat anti-mouse Alexa 568 conjugated	Thermo Fisher	RRID: AB_141371
donkey anti-goat Alexa 488 conjugated	Thermo Fisher	RRID: AB_142672
donkey anti-mouse Alexa 568 conjugated	Thermo Fisher	RRID: AB_2534013
Chemicals, Peptides, and Recombinant Proteins		
Collagenase, Type IV	ThermoFisher	Cat# 17104019
DNase I	StemCell Technologies	Cat# 07900
Tubocurarine chloride	Sigma-Aldrich	Cat# 1702008
Critical Commercial Assays		
RNAscope Multiplex Fluorescent Reagent Kit	Advanced Cell Diagnostics	Cat# 320850
RNAscope 2.5 HD reagent kit-RED	Advanced Cell Diagnostics	Cat# 322350
Papain Dissociation System	Worthington Biochemical	Cat# LK003150
Single Cell 3' Reagent Kit (v2 Chemistry)	10x Genomics	Cat# PN-120237
Experimental Models: Organisms/Strains		
Mouse: <i>Tmie-ko</i>	Zhao et al., 2014	N/A
Mouse: <i>Tmhs-ko</i>	Xiong et al., 2012	N/A
Mouse: <i>Pcdh15-av3j</i>	MGI	MGI:3581190
Mouse: <i>Vglut3-ko</i>	Jackson lab	MGI:3777618
Software and Algorithms		
R	r-project.org	R 3.3.2
Cell Ranger	10x Genomics	v1.2
Seurat	Satija Lab	v1.2
MAST	Gottardo Lab	v1.4.1
MATLAB	Mathworks	RRID:SCR_001622
Other		
Flow Cytometer	Sony	SH800
Chromium Single Cell Controller	Chromium 10x genomics	N/A

CONTACT FOR REAGENT AND RESOURCE SHARING

Requests for resources and reagents should be directed to Lead Contact Ulrich Mueller (umuelle3@jhmi.edu).

EXPERIMENTAL MODEL AND SUBJECT DETAILS

Ethic statement

IACUC Institutional Review Boards at the Johns Hopkins University School of Medicine approved all animal procedures.

Mouse strains

Tmie-ko, *Lhfpl5-ko*, *Vglut3-ko*, and *Pcdh15-av3j* mice were maintained on a C57BL/6 background and have been described previously (Alagramam et al., 2011; Borgius et al., 2010; Madisen et al., 2010; Seal et al., 2008; Xiong et al., 2012; Zhao et al., 2014).

METHOD DETAILS

Cell dissociation of SGNs for single-cell RNA-Seq

Temporal bones from 9 wko, male CBA/Caj mice ($n = 8$ capsules from 4 mice) were isolated in ice-cold Leibovitz's L-15 medium, and the overlying bone and lateral wall was extracted from apex to base, leaving just the modiolus. The remaining structures consisted of the spiral ganglion, the spiral limbus, inner sulcus, and portions of the organ of Corti and outer sulcus. Microdissected tissue from each mouse was pooled in a solution of Leibovitz containing 200 units/mL collagenase IV (Sigma) and 10 kunitz/ml DNase I (Stem Cell Technologies) and incubated for 30 min at 37°C to digest extracellular matrix. The collagenase IV solution was then replaced with EBSS containing 20 units of papain (Worthington Biochemical), 1 mM L-cysteine, 0.5 mM EDTA, 15 mM HEPES, and 10 kunitz/ml DNase I and incubated for an additional 30 min at 37°C, triturating with a 1000 µL pipette every 10 min to generate a single cell suspension. An equal volume of Leibovitz containing 20% ovomucoid protease inhibitor (Worthington Biochemical) was added, and the dissociated cells were passed through a 20 µm filter (pluriSelect) to remove large debris. The cells were pelleted at 300 g for 5 min, washed twice with PBS containing 0.04% BSA, and then pelleted and resuspended in PBS/BSA solution. Finally, a 9 µL sample of the cell suspension was counted on a Luna FI automated counter using an AO/PI cell viability assay (Logos Biosystems). Total time from euthanasia to single-cell capture was ~3 h.

Single-cell capture, library preparation, and RNA-Seq

The cell suspension was diluted to a concentration of ~500 cells per µL and immediately captured, lysed, and primed for reverse transcription (RT) using the high throughput, droplet microfluidics Gemcode platform from 10X Genomics with v2 chemistry (Zheng et al., 2017). Each droplet on the Gemcode co-encapsulates a cell and a gel bead that is hybridized with oligo(dT) primers encoding a unique cell barcode and unique molecular identifiers (UMIs) in lysis buffer. The capture process takes 6 min, after which the transcriptomes captured on gel beads are pooled and immediately reverse transcribed to cDNA. Since all cDNA is pooled and PCR amplified, cell barcodes and UMIs facilitate demultiplexing of the originating cell and mRNA transcript after sequencing. RT-PCR amplification of cDNA, and preparation of a library from 3' ends were conducted according to the manufacturer's published protocol. We performed 14 cycles of PCR amplification of cDNA. The library was sequenced on an Illumina NovaSeq 6000 with an S2 100 cycle reagent kit at the Broad Institute Sequencing Facility.

Processing and QC of single-cell RNA-Seq data

Reads were demultiplexed, aligned to the GRCm38 mm10 assembly reference genome, and filtered; and cell barcodes and UMIs were quantified using the 10X Genomics Cell Ranger pipeline with default parameters (<https://support.10xgenomics.com/single-cell-gene-expression/software/overview/welcome>). Cell Ranger uses STAR (Dobin et al., 2013) for alignment and manufacturer's software for all other steps (Zheng et al., 2017). For each gene, UMI counts of all transcript isoforms are summed to obtain a digital measure of total gene expression. Droplets containing cells are selected from empty droplets based on ranked UMI complexity of the cell barcodes. Processing the single-cell data from all four mice with the Cell Ranger pipeline resulted in a digital expression matrix of 27,998 genes by 17,900 cells.

All further filtering and downstream analysis of single-cell data described in subsequent sections was performed with Seurat v2.1, using default parameters unless specified (<https://satijalab.org/seurat/>) (Butler et al., 2018; Satija et al., 2015). To limit the influence of low complexity cells and genes, cells with fewer than 100 expressed genes (i.e., transcript count > 1), and genes with detectable expression in 10 or fewer cells were removed. This did not remove any cells from the original matrix, but it reduced the number of genes to 18,143.

Red blood cell contamination is a concern when dissociating cells from the adult cochlea since there is a large niche of erythroid cells near the bony apex. Red blood cells are highly enriched for hemoglobin transcripts, and hemoglobin protein occupies up to 98% of the red blood cell cytosol (D'Alessandro et al., 2010). Therefore, we analyzed the fraction of total transcript counts from each single cell that were comprised of transcripts from the hemoglobin genes (*Hba-a1*, *Hba-a2*, *Hbb-bh1*, *Hbb-bs*, *Hbb-bt*). Relatively few cells (< 2%) showed substantial levels of contamination (Figure S1A). Nevertheless, we removed any cell with > 5% contamination, which reduced the total number of cells to 17,556.

The resultant data was of comparable quality and complexity as other published droplet-based single-cell resources (Macosko et al., 2015; Zheng et al., 2017). QC metrics for sequencing, alignment, and quantification are listed for each mouse in Table S1. Per cell, there were $134,912 \pm 46,895$ mean reads, $5,251 \pm 1,256$ median UMIs, $2,142 \pm 396$ median genes. At this sequencing depth,

UMI complexity reached $83\% \pm 3\%$ saturation, which is well into the linear plateau of the saturation curve. [Figure S1](#) shows plots of UMI and gene complexity categorized by mouse and cluster (as defined in [Figure S2A](#)). Of note, UMI and gene complexity were noticeably bimodal ([Figure S1B](#)). A comparison of the number of UMIs and genes per cell for SGNs versus all other cell types revealed that much of the bimodality was driven by higher complexity of neurons ([Figure S1D](#)). The median number of genes per SGN was 4,202. Higher complexity of transcript species is expected for differentiated cells like neurons ([Zeisel et al., 2015](#)).

Dimensionality reduction and clustering

Full descriptions of Seurat's clustering procedure can be found at <https://satijalab.org/seurat/>. Briefly, after QC and filtering, gene expression for each cell was normalized by total transcript count, multiplied by a factor of 10,000, and log-transformed. To identify highly variable genes that account for cellular heterogeneity, genes were binned by average expression level and selected based on the z-score of their dispersion within each bin. For unbiased clustering of cells, Seurat uses a modularity-based method on shared nearest neighbor graphs, which are constructed from the Euclidean distances of reduced dimensionality space. Modularity optimization is then applied to cluster the cells, with the degree of clustering controlled by a user-defined resolution parameter. Principal component analysis (PCA) was used for dimensionality reduction and was calculated from z-scored residuals of the regressed gene expression matrix. We regressed on sample (mouse) and the number of UMIs per cell to control for unwanted variation across samples and sequencing depth. PCA was first computed for the highly variable genes then projected onto the entire matrix. For all clustering analyses, we chose twice the number of PCs at the elbow of a scree plot as input. Cluster identification was robust across a range of PCs and resolutions ([Figure S4A](#); see discussion of clustering robustness below).

Classification of type I and type II SGNs

To isolate subsets of SGNs, we performed iterative rounds of clustering and cell selection, which is a common procedure when analyzing single-cell data ([Zheng et al., 2018](#)). For the initial matrix of 17,556 cells, we identified 2,378 variable genes and 24 unique clusters using 60 PCs and a resolution of 0.3. To visualize the clusters, we computed the t-Distributed Stochastic Neighbor Embedding (tSNE) of the cells using the first 60 PCs and overlaid the cluster assignments on the first two dimensions ([Figures 1B and S2A](#)). The resultant plot showed substantial separation of the majority of the clusters. In addition, a heatmap of the top 20 genes that were unique to each cluster based on average log fold-change showed a high degree of heterogeneity between the clusters ([Figure S2B](#)). Based on expression of known marker genes, the non-neuronal clusters represented a diverse array of cell types, including hair cells, epithelial cells, immune cells, glia, mesenchymal cells, fibrocytes, and interdental cells (data not shown). As discussed in the main text, three clusters were putative type I SGNs and one cluster was putative type II SGNs ([Figures S2C and S3](#)). Since SGNs are the focus of this report, further analysis of the non-neuronal clusters is not presented.

The initial clustering analysis revealed potential subtype heterogeneity among the putative type I SGNs ([Figure S4B](#)). To eliminate unwanted sources of variation on the clustering process potentially driven by the influence of other cell types, we selected the four putative SGN groups and repeated the clustering analysis to isolate specific differences among these cells. We identified 1,634 variable genes and 10 clusters using 30 PCs and a resolution of 0.3 ([Figure S5](#)). The smallest of the ten clusters segregated on the first PC of a PCA, had low UMI complexity, and showed low expression levels of canonical SGN genes like *Nefh*, *Nefl*, and *Tubb3* (cluster 9 in [Figure S5F](#)), suggesting it was substantially different from the other SGNs. In addition, cells in this cluster expressed significantly higher levels of *Npy*, a gene which can be expressed in either neurons or glia ([Ubink et al., 2003](#)). Another cluster did express canonical SGN genes but showed elevated levels of *Coch* (cluster 6 in [Figure S5F](#)), a gene that has previously been localized to fibrocytes ([Robertson et al., 2001](#)). This cluster of cells also separated from the majority of cells on PC1. Lastly, a third cluster of cells had very low UMI complexity that was well below the median for all cells ([Figure S5E](#); cluster 7 in [Figure S5F](#)) and did not appear to express many unique genes. Based on these findings, we eliminated these three clusters ([Figure S5B](#)). Of the remaining seven clusters, one represented type II SGNs based on expression of type II SGN genes like *Prph*, and the remaining six were type I SGNs ([Figure S5F](#)). This final dataset of SGNs consisted of 6,113 type I and 95 type II cells ([Figure 1C](#)). The removed cells represented < 8% of the putative SGNs selected from the full matrix; however, it should be noted that 40% of the putative type II SGNs in [Figure 1B](#) were eliminated.

Clustering robustness

In order to evaluate the robustness of our initial clustering and identification of neuronal populations, we performed clustering on the full matrix of 17,556 cells 25 times, varying the parameters. We varied the number of principal components used from 40 to 80, and the resolution parameter from 0.2 to 0.4. After each round of clustering, we recorded the identities of type I and type II neurons, as well as the identities to which all other cells were assigned. Finally, we computed a consensus matrix, in which each value corresponds to the number of times each pair of cells was identified as the same cell type ([Figure S4A](#)). Thus, for the identification of gross neuronal identity, the clustering analysis was insensitive to a range of PCs and resolutions.

Classification of type I SGN subtypes

Both clustering analyses suggested there was additional heterogeneity among type I SGNs. To explore this further, we selected all type I SGNs from the final dataset and performed a third round of clustering. Physiological recordings indicate at least three subtypes, so we systematically altered the resolution parameter until three clusters emerged (2,282 variable genes, 22 PCs, and a resolution

parameter of 0.15). As subsequent histological validation confirmed (Figure 2), these clusters represented true biological variation and not sample bias (Figure S7A) or glial contamination (see more in-depth discussion of the effects of glia contamination below).

Increasing the resolution parameter to 0.2 led to the identification of 2 additional clusters; however, examination of marker genes (highest average log fold-change of significant genes from pairwise comparisons) revealed glia-specific genes like *Mpz*, *Pmp22*, *Mbp*, and *Mpzl1*. Thus, glial contamination appeared to be the next largest source of variation that drove clustering within the dataset. This was not surprising given that the most negative loadings on several of the PCs were glia-specific genes.

We wondered whether further biological heterogeneity existed within the dataset, and was masked by PCs representing glial contamination. In addition, since PCA only finds maximum sources of variance, each PC can potentially represent multiple cell types. Independent component analysis (ICA), on the other hand, seeks to identify basis vectors that are statistically independent, and it has been successfully employed to separate subtle differences between cells in scRNA-Seq data (Trapnell et al., 2014; Zheng et al., 2018). Therefore, we applied Seurat's clustering procedure using ICA instead of PCA. The elbow in the scree plot occurred at the eighth IC, and the gene loadings revealed that IC1 and IC8 likely represented the previously identified Type IA, B, and C clusters. Except for IC2, the remaining ICs were either glial cells or redundant. Using these ICs (1, 2, and 8), we re-clustered the cells, and found that a resolution parameter of 0.1 recapitulated the original 3 clusters with > 90% agreement (Figure S7C). Furthermore, increasing the resolution to 0.3 split the original 3 clusters into 6 (Figures S7D and S7E). Contaminating glial gene expression was evenly distributed, indicating that glial contamination did not drive clustering (Figure 7E).

Differential expression analysis

All differential expression analysis was performed using MAST (Finak et al., 2015). Briefly, we fit a two-part generalized linear model, which allowed us to model both the rate of expression of a gene over background, as well as the positive expression mean. Prior to differential expression testing, the gene expression matrix was filtered to only include genes expressed in > 5% of all cells. The sample of origin and the variable of interest (e.g., subtype) were modeled as a mixed and fixed effect, respectively. The gene complexity of each cell was also included as a fixed effect. A likelihood ratio test was used to determine the significance values, and p values were adjusted for multiple hypothesis testing using the Benjamini-Hochberg method. Genes with an adjusted p value < 0.01 and an absolute log-fold change > 0.1 were counted as significant. Significant hits from all differential expression analyses are reported in Tables S2 and S3. Table S6 lists the genes that comprise the six functional categories of molecules as described by Paul et al. (2017). The differentially expressed genes in Tables S2 and S3 were cross-referenced with this list to identify the genes shown in Figure 3A.

Effects of glial contamination

In mice, both the peripheral fibers and soma of most type I SGNs are myelinated, and the soma are also surrounded by satellite glial cells. Given the strong adhesions between these cell types, it is difficult to fully dissociate SGNs from glia. Thus, we expected that many of the droplets consisted of co-captures of neurons and glia. Indeed, the SGN clusters identified in Figures 1B and S2A had detectable levels of glia-specific transcripts like *Mpz*, *Pmp22*, *Mbp*, and *Mpzl1*, albeit the levels were significantly lower than in the cluster of pure glial cells (Figures S6A and S6B). Some cells showed less contamination than others, which contributed to the clustering presented in Figure S5A (Figures S6C and S6D).

As described above, glial contamination did not appear to contribute to the clustering type I SGNs into three major subtypes. However, to be certain of this, we selected the type I SGNs that had lower levels of glial gene contamination (i.e., clusters 4 and 5 in Figure S6C), and repeated the clustering procedure to extract three clusters from the dataset. The three clusters appeared to be grossly identical to those identified in the full dataset, and the genes that were differentially expressed between subtypes in the full and non-contaminated datasets were highly correlated (Figures S6E–S6G; Tables S4 and S5). Lastly, there was little overlap in genes that were differentially expressed between subtypes in the non-contaminated dataset compared to genes that were differentially expressed between contaminated and non-contaminated type I SGNs (Figure S6H; Tables S4 and S5). The glia specific genes identified in the latter analysis had 87% overlap with genes that were differentially expressed between all type I SGNs and pure glia (clusters 0, 1, and 4 versus cluster 2 in Figure S2A).

Immunofluorescence

For immunofluorescent studies, cochlea was dissected from mice perfused with 20 mL 0.1 M PBS (pH 7.4) followed with 25 mL of fixative (4% formaldehyde (vol/vol)). After post-fixation overnight in 4°C, tissues were decalcified in 100mM EDTA for 2-3 days, cryoprotected in 30% sucrose (wt/vol) for 12 h and then sectioned with a cryostat at 16 µm. The sections on slides were dried at 37°C for 40 min, and fixed with 4% paraformaldehyde at room temperature for 10 min. The slides were pre-incubated in blocking solution (10% normal goat serum (vol/vol), 0.2% Triton X-100 (vol/vol) in PBS, pH 7.4) for 1 h at room temperature, then incubated overnight at 4°C with primary antibodies. Secondary antibody incubation was performed at room temperature for 2 h. After rinsing in PBS, samples were coverslipped with Vectashield. Labeled sections were imaged using a Zeiss 700 Confocal Laser Microscope System.

For primary antibodies, we used goat α -CALB2 (CG1, Swant, 1:2500), mouse α -CALB2 (MAB1568, Millipore, 1:1000), mouse α -TuJ1 (801201, Biolegend, 1:400), rabbit α -TuJ1 (SAB4500088, Sigma, 1:200), mouse α -POU4F1 (MAB1585, Millipore, 1:20), rabbit α -CALB1 (13176, New England Biolabs, 1:50), rabbit α -Tyrosine Hydroxylase (657012, Millipore, 1:1000) and rabbit α -p75 NGFR (Weskamp and Reichardt, 1991, 1:800). For secondary antibodies, we used goat α -rabbit (A11008, Alexa 488 conjugated;

A11011, Alexa 568 conjugated, Thermo Fisher), goat α -mouse (A11001. Alexa 488 conjugated; A11004, Alexa 568 conjugated, Thermo Fisher), donkey α -goat (A11055, Alexa 488 conjugated) and donkey α -mouse (A10037, Alexa 568 conjugated). All secondary antibodies were diluted 1:500 in blocking solution.

Serial sections were analyzed from at least three animals for each genotype and the number of neurons expressing molecular markers was determined in each section. Data analysis was performed using Excel (Microsoft, Redmond, WA) and R (MathWorks, Natick, MA). All data are presented as mean \pm SEM. Student's two-tailed paired or unpaired t test was used to determine statistical significance between measurements in the same cohort or different cohorts, respectively (* $p < 0.05$, ** $p < 0.01$, *** $p < 0.001$). Data are also presented in the main text and in the figure legends.

RNAscope *in situ* hybridization

Fixed frozen sections were obtained as described above at 14 μ m. RNAscope Multiplex Fluorescent Reagent Kit and RNAscope 2.5 HD reagent kit-RED (Advanced Cell Diagnostics) were used according to the user manual for fixed frozen tissues. Target probes for *Lypd1*, *Calb2* and *Pou4f1* were used in experiments. Data collection, quantification and statistical analysis was carried out as described in the previous section (Immunofluorescence). Data are also presented in the main text and in the figure legends.

Electrophysiology

Cochleae were dissected from postnatal day 5-7 control (*Tmie*^{+/+} or $+/-$; *Vglut3*^{+/+} or $+/-$), *Tmie*-ko, and *Vglut3*-ko mice, as described previously (Tritsch et al., 2007; Zhang-Hooks et al., 2016), in ice-cold, sterile-filtered HEPES-buffered artificial cerebrospinal fluid (aCSF) consisting of the following (in mM): 130 NaCl, 2.5 KCl, 10 HEPES, 1 NaH₂PO₄, 1.3 MgCl₂, 2.5 CaCl₂, and 11 D-Glucose. Explants were mounted onto Cell-Tak (Corning) treated coverslips and incubated at 37°C for 24 hr in Dulbecco's modified Eagle's medium (F-12/DMEM; Invitrogen) supplemented with 1% fetal bovine serum (FBS) and 10U/mL penicillin (Sigma) prior to recording.

For juxtacellular recordings, cochleae were transferred to a recording chamber and continuously superfused with bicarbonate-buffered aCSF at 1.5 - 2 mL/min, consisting of the following (in mM): 115 NaCl, 6 KCl, 1.3 MgCl₂, 1.3 CaCl₂, 1 NaH₂PO₄, 26.2 NaHCO₃, 11 D-glucose, and saturated with 95% O₂ / 5% CO₂ to maintain a pH of 7.4. Recordings were performed at near physiological temperature (32-34°C) using a feedback-controlled in-line heater (Warner Instruments). Electrodes for SGN recordings had tip resistances between 1.5-2.5 M Ω when filled with artificial cerebrospinal fluid. Extracellular potentials were recorded for 10 min with pClamp10 software using a Multiclamp 700B amplifier, low pass filtered at 20 kHz, and digitized at 50 kHz with a Digidata 1322A analog-to-digital converter (Axon Instruments). SGNs that displayed tonic firing indicative of cellular pathology were not included in the analysis datasets. For d-tubocurarine (d-TC) experiments, spikes were analyzed in five-minute windows; 5 min of baseline preceded 10 min of superfusion of aCSF containing 50 μ M d-TC and a ten-minute wash period. Firing behavior in the latter 5 min of baseline, drug and wash were analyzed.

Data were analyzed offline using custom routines written in MATLAB 2017b (Mathworks). Briefly, raw traces were high-pass filtered to remove baseline drift and spikes were identified using an amplitude threshold criterion. As described previously (Tritsch et al., 2010), bursts were identified by classifying interspike intervals into non-bursting intervals (> 1 s), burst intervals (30 ms - 1 s), and mini-burst intervals (< 30 ms). Bursts were defined as clusters of at least 10 consecutive burst intervals (with mini-burst intervals being ignored in the context of burst detection). Spikes within mini-bursts were included when calculating the number of spikes within a burst. Colored raster plots were generated by grouping spikes into one-second bins and applying a color map to the resulting data (modified 'hot' colormap; MATLAB). All values are mean \pm SEM. Statistical significance was calculated with two-tailed paired t test, Bonferroni correction applied; ** $p < 0.01$, * $p < 0.05$, ns: not significant. Data are also presented in the main text and in the figure legends. The exact number of cells analyzed is indicated in Figure 7.

DATA AND SOFTWARE AVAILABILITY

All software tools can be found online (see [Key Resources Table](#)). The accession number for the raw data files reported in this paper is GEO: GSE114759. Data are also available at gEAR (<https://umgear.org>).

Supplemental Figures

Cell

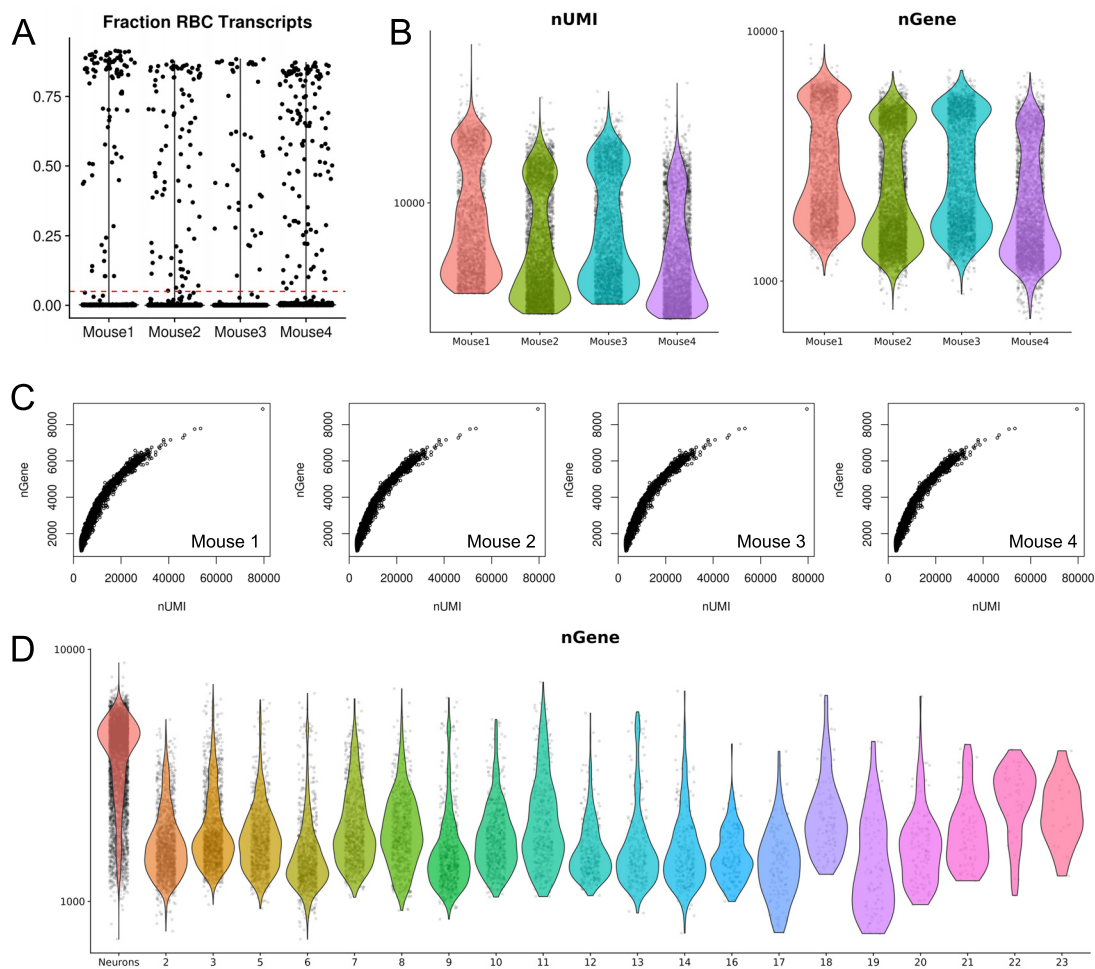


Figure S1. Quality Control and Filtering of Data, Related to Figure 1

- (A) Assessment of red blood cell (RBC) contamination for each single-cell transcriptome. Plots of the fraction of total transcript counts that were comprised of hemoglobin transcripts (*Hba-a1*, *Hba-a2*, *Hbb-bh1*, *Hbb-bs*, *Hbb-bt*) for all single cells from each mouse. Red dashed line indicates cutoff fraction (0.05) above which single cells were considered “contaminated” and were excluded from analysis (344 cells out of 17,900).
- (B) Violin plots of the number of unique molecular identifiers (nUMI) and number of genes (nGene) detected per single cell from each mouse. y axis on log10 scale.
- (C) Plots of the relationship of nUMI versus nGene per single cell for each mouse.
- (D) Violin plots of nGene detected per single cell for each cluster identified from [Figures 1B](#) and [S2A](#). Clusters 0, 1, 4, and 15 comprise the “Neurons” group.

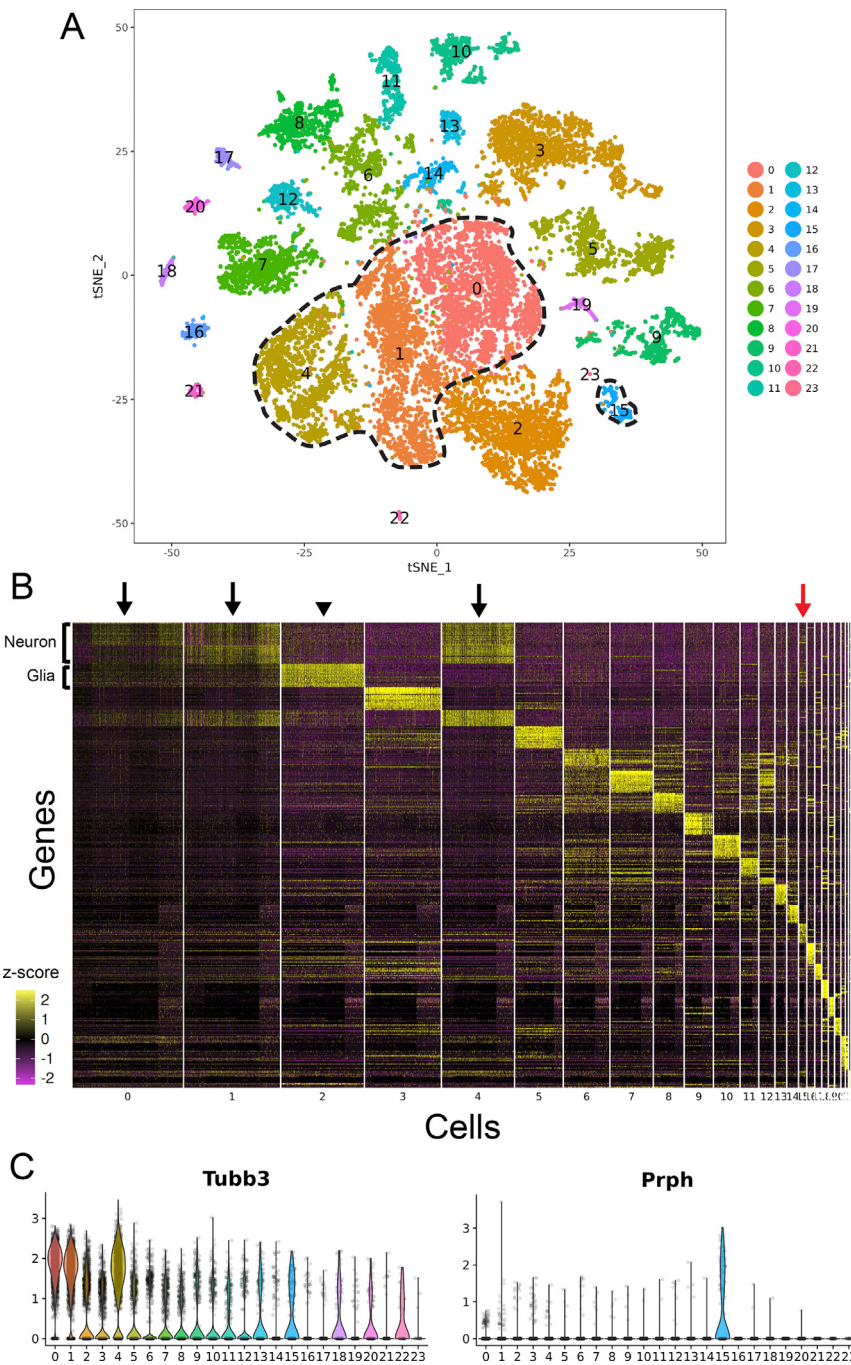


Figure S2. Cell Type Diversity and Bioinformatic Separation of Neurons from Other Cell Types, Related to Figure 1

(A) tSNE plot from Figure 1B showing the three clusters (0, 1, 4) comprising putative type I neurons and the one cluster (15) comprising putative type II neurons.

(B) Heatmap of standardized expression for the top 20 marker genes ($p < 0.01$ from pairwise comparisons, highest average log-fold change) identified for each of the 24 clusters. Genes are in rows, single cells in columns. Clusters are ordered by abundance of each cell type within the dataset. Black arrows indicate type I neurons, black arrowhead indicates glia, red arrow indicates type II neurons.

(C) Violin plots of expression for the type I marker, *Tubb3*, and the type II marker, *Prph*, for each of the neuronal clusters in relation to all other cell types.

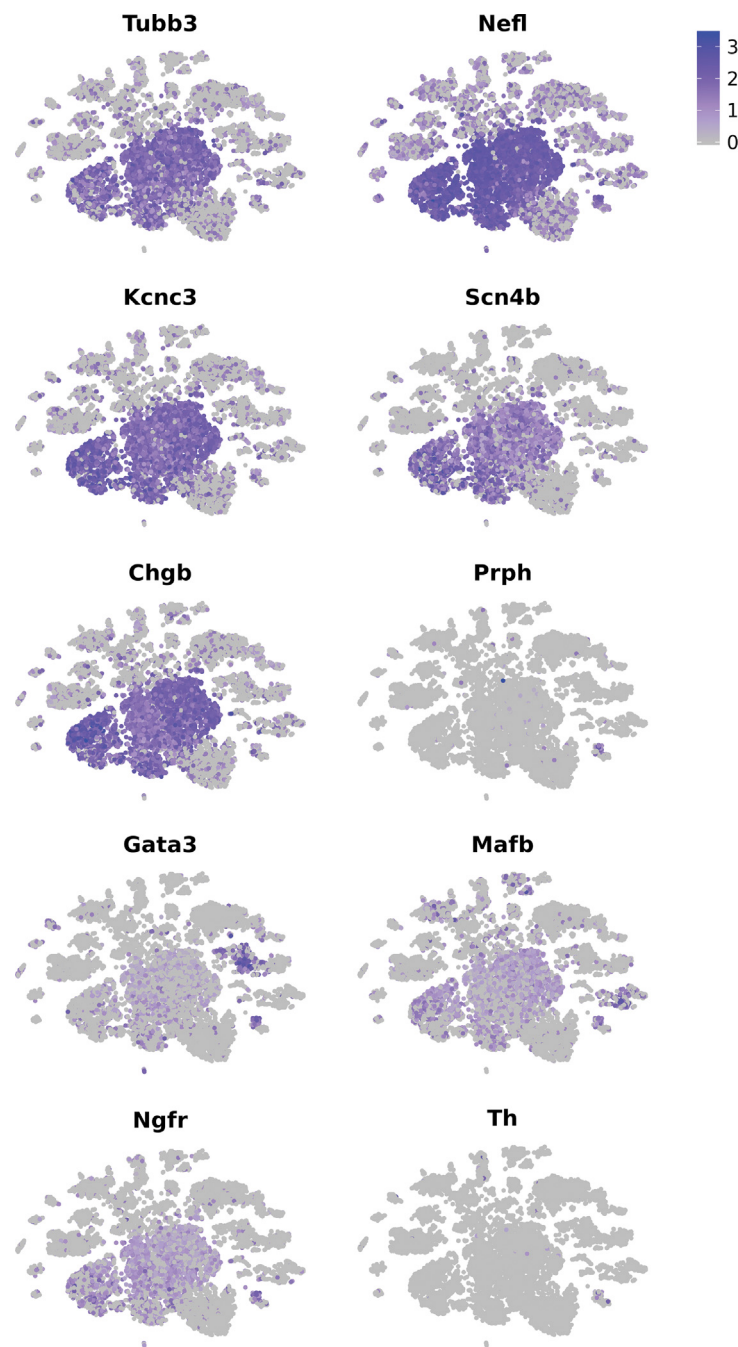


Figure S3. Specificity of Neuronal Marker Gene Expression, Related to Figure 1

Expression of marker genes from Figure 1C projected onto tSNE plot from Figure 1B. Color scale indicates log-normalized transcript counts.

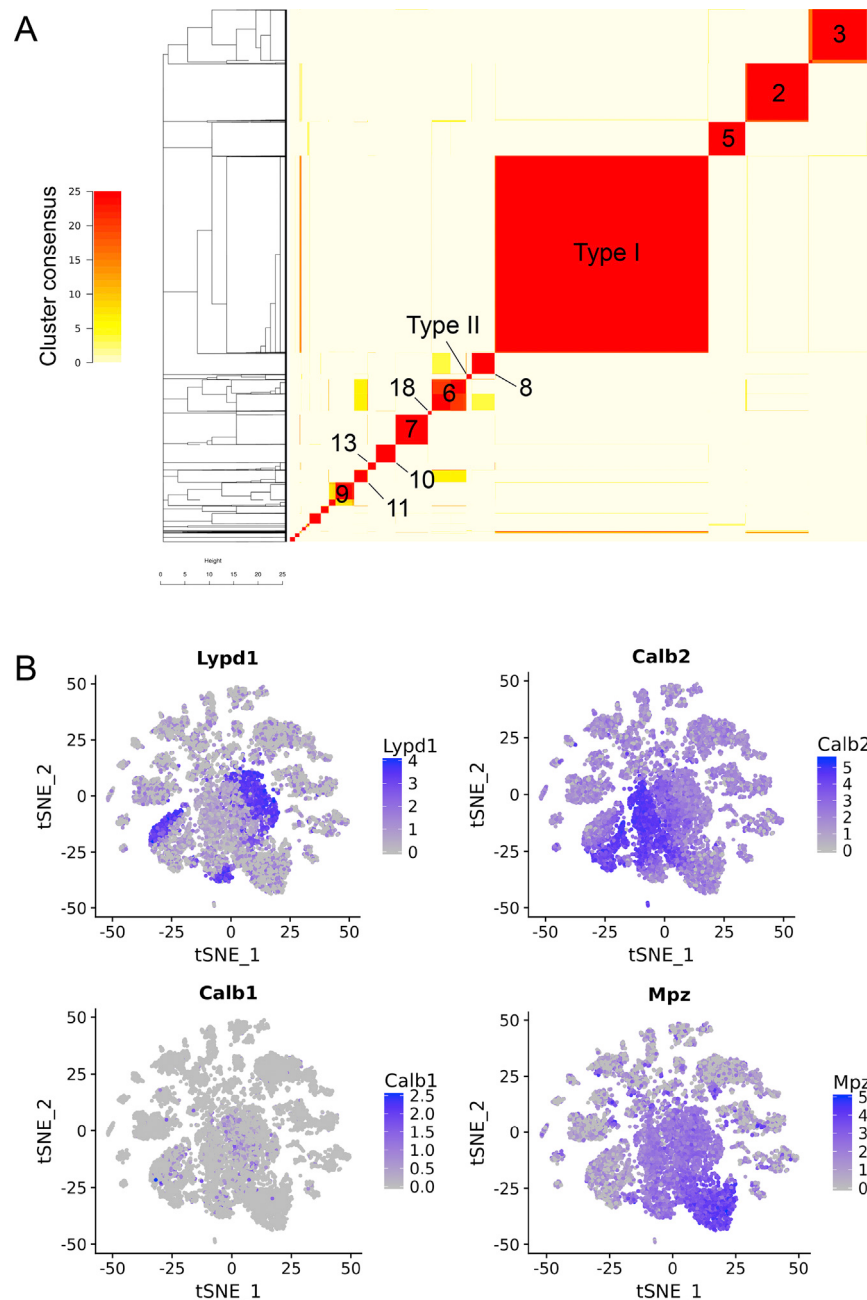
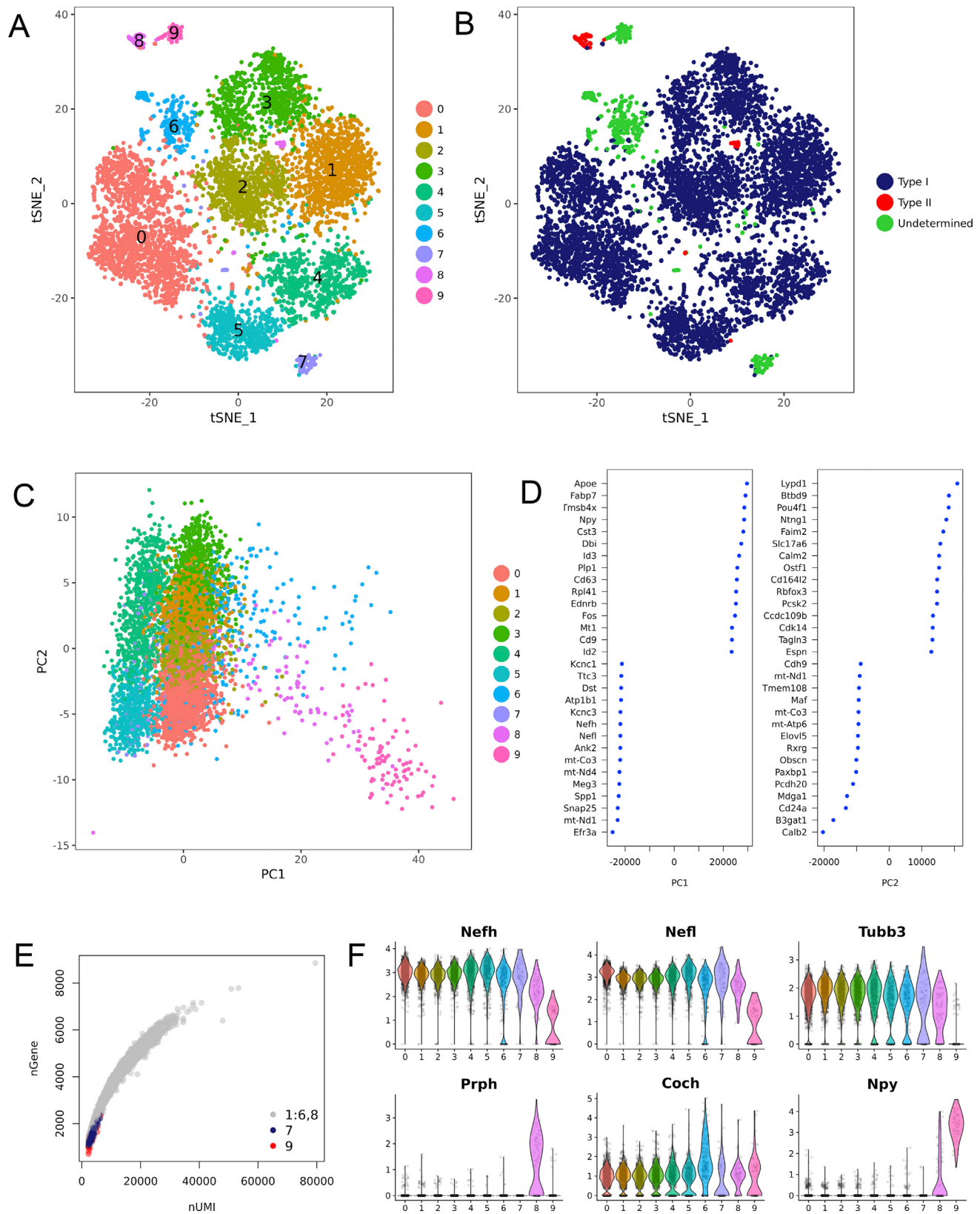


Figure S4. Robustness of Clustering and Bioinformatic Separation of Neurons, Related to Figure 1

(A) Consensus matrix from multiple clustering analyses of all cells. 25 clusterings were performed using 5 different numbers of input principal components (40 to 80) and 5 resolution parameters (0.2 to 0.4). The principal components spanned two-fold from the bend in an elbow plot of percent variance explained by each principal component.

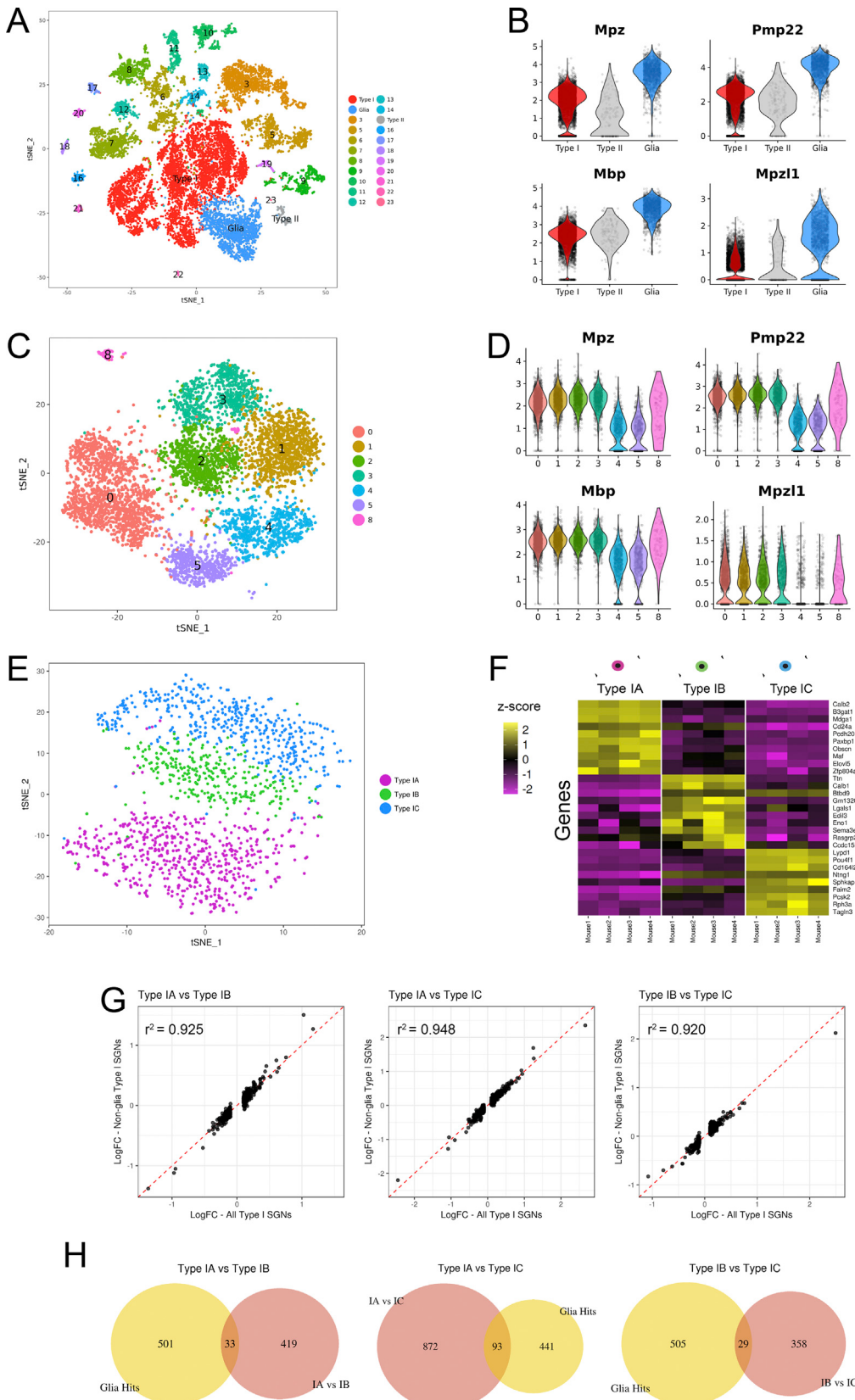
(B) Expression of type I subtype marker genes from Figures 1E and 1F projected onto tSNE plot from Figure 1B. Color scale indicates log-normalized transcript counts.



(legend on next page)

Figure S5. Filtering Undetermined Cell Types from the Neuron Clusters, Related to Figure 1

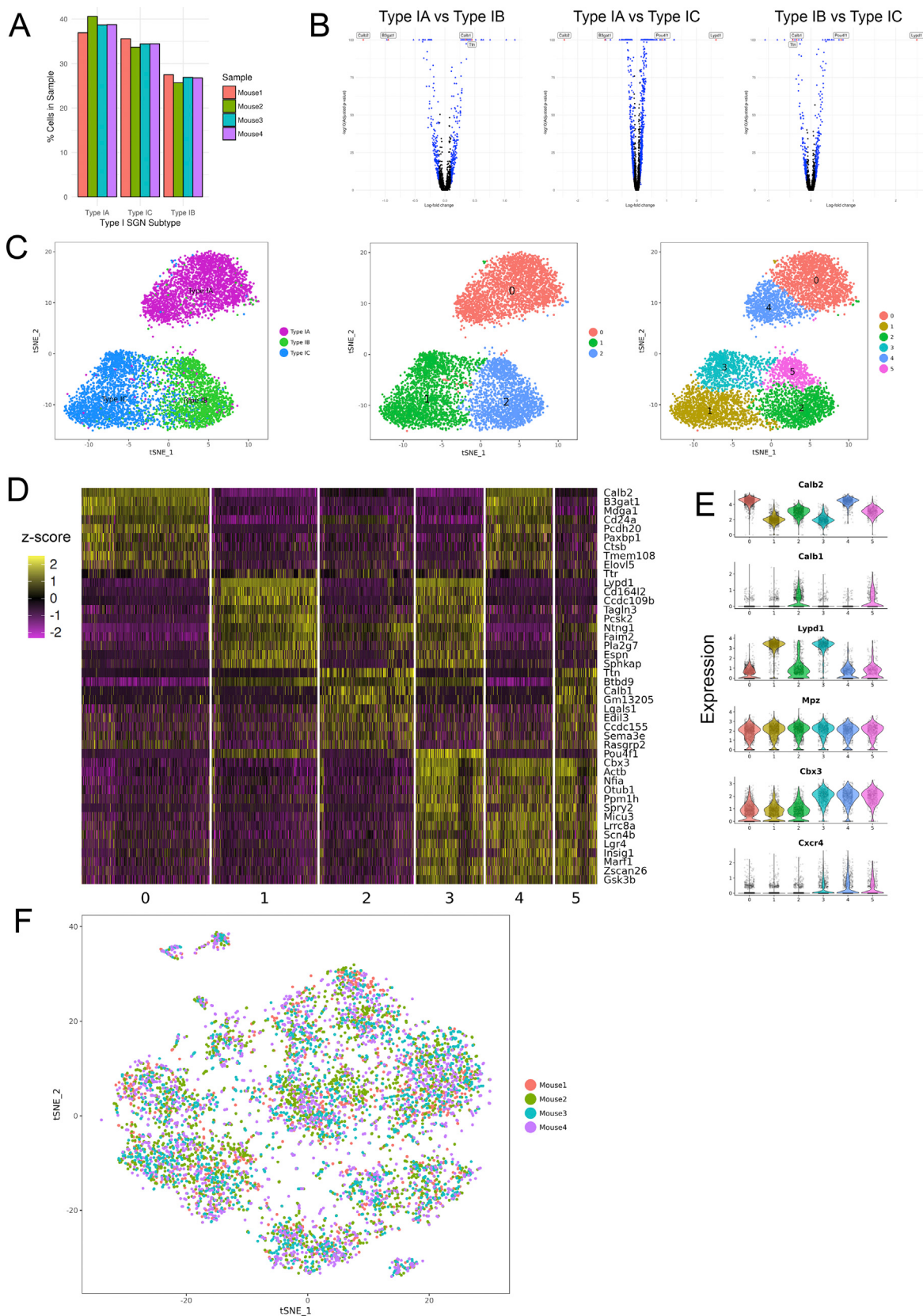
- (A) tSNE plot showing re-clustering of the putative neurons identified in [Figures 1B](#) and [S2A](#).
- (B) tSNE plot showing clusters selected for final type I and type II SGN dataset (0–5, 8) and clusters with uncertain or undetermined identities (6, 7, 9).
- (C) Plot of first two principal components showing how the clusters in (A) segregate.
- (D) Top 15 positive and negative gene loadings from PC1 and PC2.
- (E) Plot of number of genes versus number of UMIs per single cell for all the cells shown in (A). Cells from clusters 7 (blue) and 9 (red) are highlighted.
- (F) Violin plots of canonical SGN markers (*Nefh*, *Nefl*, *Tubb3*, *Prph*) and genes enriched in clusters 6 (*Coch*) and 9 (*Npy*).



(legend on next page)

Figure S6. Glial Cell Contamination, Related to Figure 1

- (A) tSNE from [Figure 1B](#) highlighting putative type I SGNs (red), type II SGNs (gray), and pure glial cells (blue).
- (B) Violin plots of glia-specific genes in the type I SGN, type II SGN, and glia clusters highlighted in (A).
- (C) tSNE plot from [Figure S5A](#) with undetermined clusters removed.
- (D) Violin plots of glia-specific genes in the clusters shown in (C).
- (E) tSNE plot showing re-clustering and identification of three major subtypes using SGNs with low levels of glial contamination (clusters 4 and 5 in [Figures S6C](#) and [S6D](#)).
- (F) Heatmap of average, standardized gene expression (rows) for the single cells from each cluster in (E) (average is displayed for each mouse). Genes are the same as those shown in [Figure 1E](#).
- (G) Plots comparing log fold-change (logFC) in gene expression for genes identified as differentially expressed (absolute logFC > 0.1 and p < 0.01) between the three type I SGN subtypes in the combined type I SGN dataset (x axis; all clusters in C) and the SGNs with low levels of glial contamination (y axis; clusters 4 and 5 in C). Pearson's correlation coefficient is shown for each comparison.
- (H) Venn diagrams comparing overlap in genes identified as differentially expressed between type I SGN subtypes, and type I SGNs with low levels of glial contamination (clusters 4 and 5 in C) versus type I SGNs with glial contamination (clusters 0, 1, 2, and 3 in C).



(legend on next page)

Figure S7. Molecular Diversity in Type I SGNs, Related to Figure 1

- (A) Distribution of cells belonging to each type I SGN subtype, categorized by sample (mouse).
- (B) Volcano plots showing results from pairwise comparisons of the type I SGN subtypes. Differentially expressed genes ($\log FC > 0.1$ and $p < 0.01$) are shown in blue. Example top differential genes are indicated in red.
- (C) tSNE plots showing clustering of type I SGNs using 22 PCs and a resolution parameter of 0.15 (left), 3 ICs and a resolution parameter of 0.1 (middle), and 3 ICs and a resolution parameter of 0.3 (right). The clusters shown on the left are identical to the clusters in [Figure 1D](#).
- (D) Heatmap showing standardized expression of the top 10 marker genes in the 6 clusters identified in [Figure S7C](#) (right). Genes are in rows and single cells in columns. The three subtypes identified in [Figures 1D–1F](#) are still apparent. Group IA is represented by clusters 0 and 4; IB is 2 and 5; and IC is 1 and 3.
- (E) Violin plots showing expression of example genes in the six clusters identified in (D). Y-axes are log-normalized transcript counts.
- (F) tSNE of the putative neurons identified in [Figure 1B](#), colored by mouse of origin.